

Understanding Flow Behaviors of Supercooled Liquids by Embodying Solid-Liquid Duality at Particle Level

Dong-Xu Yu, Ke-Qi Zeng, and Zhe Wang*

*Department of Engineering Physics and Key Laboratory of Particle and Radiation Imaging
(Tsinghua University) of Ministry of Education, Tsinghua University, Beijing 100084, China*

(Dated: June 9, 2025)

Supercooled liquids exhibit intricate flow behaviors, which progressively become nonlinear as flow rate increases. Conceptually, this complexity can be understood by the *solid-liquid duality* in Maxwell's understanding of materials' response to external load. Nevertheless, the microscopic foundation of this duality in supercooled liquids remains elusive, thereby impeding the modeling of flow behaviors from a microscopic viewpoint. The existence of dynamic heterogeneity adds to this difficulty. To tackle these problems, we propose the concept of local configurational relaxation time τ_{LC} , which is defined at the particle level. The spatial distribution of τ_{LC} in flow is heterogeneous. Depending on the comparison between the local mobility measured by τ_{LC} and the external shear rate, the shear response of local regions is either solid-like or liquid-like. In this way, τ_{LC} plays a role similar to the Maxwell time. By applying this microscopic solid-liquid duality to different conditions of shear flow with a wide range of shear rates, we describe the emergence of shear thinning in steady shear, and predict the major characteristics of the transient response to start-up shear. Furthermore, we reveal a clear structural foundation for τ_{LC} and the solid-liquid duality associated with it by introducing an order parameter extracted from local configuration. Thus, we establish a framework that connects microscopic structure, dynamics, local mechanical response, and flow behaviors for supercooled liquids. Finally, we rationalize our framework by leveraging the connection among structure, dynamics, and potential energy landscape (PEL). The PEL model illustrates how local structure, convection and thermal activation collectively determine τ_{LC} . Notably, it predicts two distinct response groups, which well correspond to the microscopic solid-liquid duality.

I. INTRODUCTION

In 1867, James C. Maxwell proposed a simple model that contains the essential ingredients of viscoelasticity [1]. Combining a perfectly elastic element with a perfectly viscous element in series, this model defines a characteristic relaxation time τ_M , now known as the Maxwell time, which is pivotal in ascertaining the response of materials to external load. For external loads much faster than τ_M , the material is unable to relax promptly and exhibits solid-like behavior. Conversely, for loads much slower than τ_M , the material responds as a viscous liquid. To generalize this simple picture to the vast range of viscoelastic materials, one way is to employ macroscopic laws and phenomenological construction [2, 3]. The former includes laws in thermodynamics and continuum mechanics, and symmetry arguments. For the latter, the most typical example is serial or parallel combination of Maxwell units with certain relaxation spectrum. Despite the widespread success, this approach is limited by its lack of microscopic foundation. Consequently, the range of application and generality of such models are difficult to justify.

To overcome the aforementioned challenge, one needs to embody Maxwell's picture of the solid-liquid duality at the microscopic level. Here, the key question is to identify the microstructure that determines the deformation and its relaxation time. A celebrated example of this mi-

croscopic approach is the tube model of entangled polymers established by Edwards, de Gennes and Doi [4–6]. In this model, many-body distribution and interaction of polymer chains are abstracted to a virtual tube. Due to the constraint of the tube, the chain performs curvilinear diffusion along the tube axis, called reptation, with a microscopic relaxation time τ_d that characterizes the escape process of the chain from its original tube. τ_d plays a role as the Maxwell time, in the sense that for deformation faster than the escape, the entangled polymer melt behaves elastically as a rubber, while for deformation slower than the escape, the system behaves as a viscous liquid. The clear-cut molecular basis of τ_d directly leads to the relation connecting τ_d to the microstructural property: $\tau_d \propto Z^3$, where Z is the number of entanglement per chain [6]. In the nonlinear rheological regime, strong convective effects, such as convective constraint release [7] and chain stretching [8, 9], are influential to chain relaxation. Nevertheless, the concept of reptation and τ_d are still applicable, and play a crucial role in determining the chain orientation in flow [9].

For simple liquids [10], Maxwell's idea has also been introduced to describe the microscopic dynamics [11–13]. For instance, by constructing a frequency-dependent viscosity with τ_M , one obtains the viscoelastic approximation for transverse-current correlation function [10, 12]. It works well at the molecular level for hard-sphere fluids with moderate densities, while for supercooled states where the viscoelasticity becomes significant, this approximation breaks down. A pronounced challenge for applying Maxwell's picture to the supercooled state is the dynamic heterogeneity (DH) [14–18], which implies

* zwang2017@mail.tsinghua.edu.cn

that different regions in a supercooled liquid exhibit different mobilities. Such spatially heterogeneous mobility renders the global relaxation time ineffective at the local scale [19, 20]. To tackle this problem, one may assign a spatially varying relaxation time [13], whereas the way to extract such local relaxation time can be tricky: It is found that definitions of local time from different considerations may lead to different conclusions even at qualitative level [21, 22]. This problem becomes more complicated when the external flow is applied. In this case, the relaxation of local configuration is a result of the combined effect of thermal activation and convection [23]. Therefore, a proper definition of local characteristic time is expected to distinguish between these two effects.

Concerning DH, it has long been argued that the local dynamics can be well predicted by local configuration for supercooled liquids and glasses [24–37]. Particularly, some local structural parameters exhibit predictive ability for a wide range of temperatures and densities, and for both quiescent state and states under external load [26–28, 30, 31, 33]. Considering these progresses, we expect that the aforementioned local characteristic time in supercooled liquids, which determines the local response to load, is strongly correlated to the local configuration. This correlation, if exists, has a further meaning. Unlike polymers, emulsions, foams, microgels and other soft materials composed of mesoscopic soft units [2, 3, 6, 23, 38–41], the constituent particle of simple liquids itself does not contribute elasticity. Thus, the viscoelasticity of supercooled simple liquids originates from collective behaviors of particles [42, 43], which is believed to be related to the local configuration, such as packing and orientation [26, 44–46]. Establishing this correlation is important for clarifying how the rheological response is determined by the mesoscopic structure and collective behaviors of particles. Moreover, the definition of such local time and its relation to local configuration should be general enough: they should be applicable to various flow conditions and a broad range of flow rates including the Newtonian regime and the nonlinear regime.

In this paper, we provide an understanding of the shear rheology of supercooled liquids by embodying Maxwell’s picture of solid-liquid duality at the particle level. With non-equilibrium molecular dynamics (MD) simulations, we introduce the concept of local configurational relaxation time τ_{LC} , which can be measured once a microscopic configuration is given, regardless of whether the system is in an equilibrium state or under shear. τ_{LC} varies in space in the same way as the commonly-understood DH. The competition between the local mobility represented by τ_{LC} and the external strain rate determines how the local structure responds to shear, namely, solid-like or liquid-like. In this way, τ_{LC} plays a role similar to that of τ_M in the Maxwell model. By applying this space-dependent solid-liquid duality, we are able to quantitatively understand the rheological response of supercooled liquids to both steady shear and start-up shear in a broad range of shear rates. We in-

troduce τ_{LC} in Sec. II, and discuss the flow behaviors of supercooled liquids based on τ_{LC} in Sec. III.

Furthermore, we reveal a robust correlation between τ_{LC} and microscopic structural features. Our findings suggest a firm relation between relevant local structural parameters and τ_{LC} , irrespective of shear rates. Based on this correlation, we define a structural order parameter, which effectively distinguishes whether the local response to shear is liquid-like or solid-like. Combining these efforts and the results in Secs. II and III, we bridge the gap between microscopic structure and macroscopic rheology—a long-standing objective in soft condensed matter physics [2, 6, 38]. These results are given in Sec. IV.

In addition, we attempt to formulate the connection from microscopic structure to flow behaviors established in Secs. II – IV by employing the concept of potential energy landscape (PEL) [47–50]. Within the PEL framework, we illustrate the physical significance of τ_{LC} and how it is determined by the collective effect of local structure, convection, and thermal activation. Moreover, we elucidate the mechanism of the solid-liquid duality in response and its consequence in the emergence of nonlinear flow behaviors. The relevant discussion is given in Sec. V.

II. LOCAL CONFIGURATIONAL RELAXATION TIME

A. Simulation method

Three-dimensional MD simulations utilizing cubic periodic boundary conditions are employed to investigate the flow of supercooled liquids. Binary mixtures are adopted to prevent crystallization [51]. The mixture is composed of 80% big particles (denoted by subscript “b”) and 20% small particles (denoted by subscript “s”) with the same mass m . The inter-particle interaction is given by the Lennard-Jones (LJ) potential $V(r) = 4\epsilon_{\alpha\beta} [(\sigma_{\alpha\beta}/r)^{12} - (\sigma_{\alpha\beta}/r)^6]$ with $\alpha, \beta \in \{b, s\}$. The LJ parameters are set as follows: $\epsilon_{bb} = 1$, $\sigma_{bb} = 1$ between big particles; $\epsilon_{bs} = 1.5$, $\sigma_{bs} = 0.8$ between big and small particles; $\epsilon_{ss} = 0.5$, $\sigma_{ss} = 0.88$ between small particles. The units of energy, length, time, and temperature are, respectively, set by ϵ_{bb} , σ_{bb} , $\sqrt{m\sigma_{bb}^2/\epsilon_{bb}}$, and ϵ_{bb}/k_B , where k_B is the Boltzmann constant. With these basic units, the units of stress and viscosity are set by $\epsilon_{bb}/\sigma_{bb}^3$ and $\sqrt{m\epsilon_{bb}/\sigma_{bb}^2}$, respectively. The potential interaction range is truncated and shifted at 2.5. To apply shear, the SLLOD equation combined with Lees-Edwards boundary condition is used [52–54]. The time step is set to 0.005. Constant NVT integration with a Nose-Hoover thermostat is employed to update positions and momenta of particles, with the application of the LAMMPS package [55].

Two samples are studied here. Sample A consists of 10976 particles with a number density of $\rho = 1.38$ and a temperature of $T = 1.0$. Sample B consists of 9000

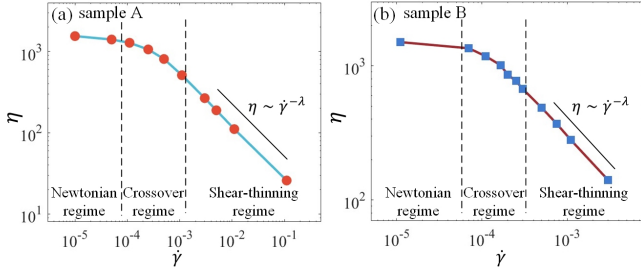


FIG. 1. Shear viscosity η as a function of shear rate $\dot{\gamma}$ for sample A (a) and sample B (b). Symbols denote the results obtained from MD data. Lines are to guide eyes. Three distinct rheological regimes can be delineated, as indicated by the vertical black dashed lines. In the shear-thinning regime, the relation can be described by a power law $\eta \sim \dot{\gamma}^{-\lambda}$.

particles with $\rho = 1.2$ and $T = 0.48$. The temperatures and number densities are carefully adjusted to ensure that both the Newtonian regime and the nonlinear regime can be achieved without too much computational cost. Under the shear with the stream velocity along the x direction, the velocity gradient along the y direction, and the shear rate $\dot{\gamma}$, the shear viscosity η is calculated by:

$$\eta = -\frac{1}{V\dot{\gamma}} \left\langle \sum_{i=1}^N r_{i,x} f_{i,y} \right\rangle, \quad (1)$$

where V is the system volume, N is the particle number, $r_{i,x}$ is the x component of the position vector of particle i , and $f_{i,y}$ is the y component of the force exerted on particle i . Figure 1 shows the viscosities of both samples under steady shear with various shear rates. At large enough $\dot{\gamma}$, both samples exhibit significant shear thinning, which can be expressed by $\eta \sim \dot{\gamma}^{-\lambda}$ [38]. The values of λ are, respectively, 0.67 and 0.66 for sample A and sample B. For the sake of convenience, we will call the regime featured by $\eta \sim \dot{\gamma}^{-\lambda}$ as the shear-thinning regime, and call the regime between Newtonian regime and the shear-thinning regime as the crossover regime. These rheological regimes are denoted in Fig. 1.

B. τ_{LC} in quiescent state and local response to start-up shear

In supercooled liquids, a particle is strongly restricted by the cage formed by its neighboring particles [56, 57]. Consequently, a particle vibrates inside its cage for most of the time, and occasionally undergoes a cage jump [58]. Knowing particle trajectories, cage jump events can be identified by the algorithm proposed by Candelier et al. [59, 60]. With this method, one can find the time before the first jump from a given time origin for a reference particle τ_p . Here, the subscript “p” denotes “persistence”, in the sense that this definition is consistent with the persistence time in continuous time random walk

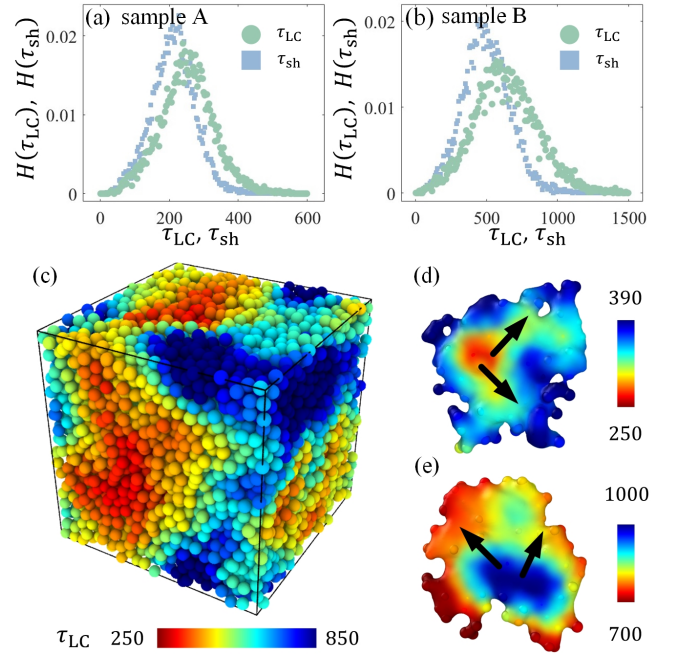


FIG. 2. (a) Normalized spectra of τ_{LC} ($H(\tau_{LC})$) and τ_{sh} ($H(\tau_{sh})$) of sample A. (b) Normalized spectra of τ_{LC} ($H(\tau_{LC})$) and τ_{sh} ($H(\tau_{sh})$) of sample B. In both (a) and (b), τ_{LC} is measured at equilibrium, while τ_{sh} is measured under the start-up shear condition with $\dot{\gamma} = 0.00025$ for sample A and $\dot{\gamma} = 0.00011$ for sample B. (c) Snapshot of the spatial distribution of τ_{LC} of sample B at equilibrium. (d) and (e) illustrate the hierarchical feature of the spatial distribution of τ_{LC} . (d) gives a slice of a fast cluster. It is seen that particles gradually become slower as the distance from the fast center grows. (e) gives a slice of a slow cluster. It is seen that particles gradually become faster as the distance from the slow center grows. Black arrows in (d) and (e) are to guide eyes, indicating that fast particles tend to “grow” from a fast center (d), and slow particles tend to “grow” from a slow center (e).

framework [61, 62]. To enhance the statistics, we employ the isoconfigurational ensemble (ICE) [63], which consists of multiple trajectories from the same configuration but with random initial momenta sampled from the Maxwell-Boltzmann distribution. Note that, by averaging across ICE, one suppresses the uncertainty related to thermal fluctuations. Thus, the ICE-averaged result $\langle \tau_p \rangle_{ICE}$ is mainly determined by the configuration at the given time origin, and is irrelevant to the instantaneous momenta. For this reason, we name it local configurational relaxation time, and denote it as τ_{LC} . Figure 2 (a) and (b) display the normalized equilibrium spectra of τ_{LC} of sample A and sample B, respectively. The value of τ_{LC} varies from particle to particle, and exhibits significant spatial heterogeneity, as shown in Fig. 2 (c) for sample B at the equilibrium state.

In principle, τ_{LC} , which represents the local relaxation rate, is relevant to the local response to external load. To explore the relation between τ_{LC} and local response, we apply the start-up shear to the equilibrium state, and

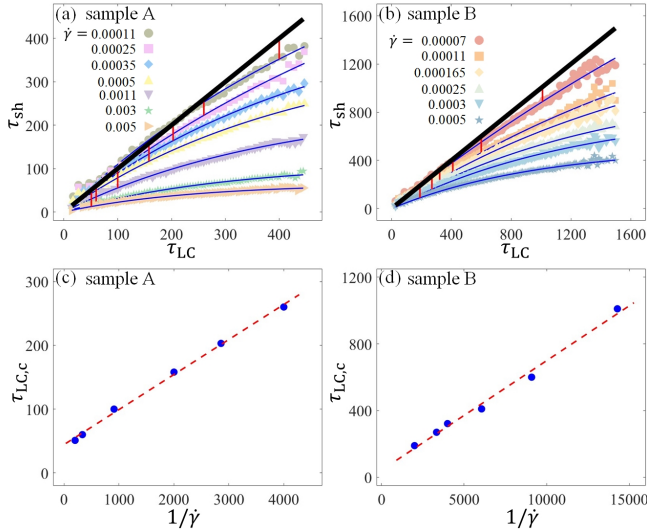


FIG. 3. (a) and (b) display the relations between τ_{LC} and τ_{sh} , denoted as $\tau_{sh}(\tau_{LC})$, obtained from start-up shear with various $\dot{\gamma}$ for sample A and sample B, respectively. In both (a) and (b), symbols denote the results, thick black lines denote the reference condition of $\tau_{sh} = \tau_{LC}$, thin blue lines denote the exponential fits for data, the positions of red vertical bars denote the boundaries between fast and slow groups $\tau_{LC,c}$, and the length of red vertical bars denotes the value of τ_2 . (c) and (d) display the boundaries between the fast and slow groups $\tau_{LC,c}$ as a function of $\dot{\gamma}^{-1}$ for sample A and sample B, respectively. In both (c) and (d), symbols denote the results, dashed lines denote the linear fits to data points.

record the first-jump time from the starting time of this shear for each particle $\tau_{p,sh}$, where the subscript “sh” represents “shear”. Then, we still perform the ICE average on $\tau_{p,sh}$ with respect to the configuration at the start of shear, and denote the result as τ_{sh} ($\tau_{sh} = \langle \tau_{p,sh} \rangle_{ICE}$). In Fig. 2 (a) and (b), we plot the distribution of τ_{sh} at a given $\dot{\gamma}$ for sample A and sample B, respectively. Compared with τ_{LC} , the distribution of τ_{sh} shifts to lower values, manifesting the facilitation of dynamics by the external shear. For a specific particle, the difference between τ_{sh} and τ_{LC} reflects the impact of shear on its mobility. Intuitively, slow particles, i.e., particles with large τ_{LC} , are more susceptible to imposed shear. On the other hand, particles with very small τ_{LC} cannot perceive the shear effect, because their spontaneous relaxations are faster than the shear rate.

To quantitatively evaluate the difference between τ_{sh} and τ_{LC} , we perform the following two-step operation for each sample: First, we divide all particles into many bins according to the ascending sequence of τ_{LC} . In each bin, particles are approximately equal in the value of τ_{LC} with a difference up to the bin width. Subsequently, for each bin, we calculate the averaged τ_{sh} for particles within that bin. With this operation, we can compare the bin-averaged values of τ_{sh} and τ_{LC} . The results, shown in Fig. 3 (a) and (b) for both samples and various $\dot{\gamma}$, can be summarized as follows: (1) For

small $\dot{\gamma}$, τ_{sh} is approximately equal to τ_{LC} for the majority of τ_{LC} values, as indicated by the close alignment with the black thick line denoting $\tau_{sh} = \tau_{LC}$. (2) As $\dot{\gamma}$ increases, deviation from this alignment grows at large values of τ_{LC} , suggesting that more and more particles are accelerated by shear. This deviation is pronounced in the shear-thinning regime, manifested by the flattening of the $\tau_{sh}(\tau_{LC})$ curve. These results are consistent with our intuition.

Knowing the relation between τ_{sh} and τ_{LC} at a specific $\dot{\gamma}$, we can categorize all particles into a *fast* group and a *slow* group, depending on the extent to which the particle is facilitated by shear. The aim of this dichotomy is to draw a correspondence to the solid-liquid duality in the Maxwell model, as we will discuss later. Here, we identify a particle as a slow one if its first-jump time in shear (τ_{sh}) is significantly accelerated compared with its equilibrium counterpart (τ_{LC}):

$$\tau_{LC} - \tau_{sh} \geq \tau_2, \quad (2)$$

where τ_2 is the non-Gaussian time at equilibrium, which measures the waiting time for the system to exhibit significant DH [64]. According to the preceding criterion, slow particles exhibit distinct relaxation heterogeneity compared with the equilibrium situation, thereby being considered as being strongly influenced by shear. Then, the fast particles are identified by satisfying $\tau_{LC} - \tau_{sh} < \tau_2$. The boundary between fast and slow groups $\tau_{LC,c}$ ($\tau_{LC,c} = \tau_{sh} + \tau_2$) is denoted by red vertical bar for each $\dot{\gamma}$ in Fig. 3 (a) and (b), where the length of the bar is set to τ_2 . $\tau_{LC,c}$ reflects the time scale of external shear, so that it is expected to linearly depend on $\dot{\gamma}^{-1}$ [65]. This linearity is shown in Fig. 3 (c) and (d), implying that our way of determining $\tau_{LC,c}$ is reasonable.

The spatial distribution of fast or slow particles and its variation with $\dot{\gamma}$ are of particular importance for clarifying the local response. To understand this point, we first notice that the distribution of τ_{LC} is hierarchical. Taking fast particles as an example: Fast particles tend to aggregate, as a manifestation of DH. The center of an aggregation is formed by a few very fast particles. As the distance from the center increases, the particles gradually become slower, as shown in Fig. 2 (d). This is consistent with the dynamic facilitation mechanism, which suggests that local relaxation events propagate to neighboring regions [59, 60, 66, 67]. Similarly, slow particles exhibit clustering with centers formed by a few very slow particles. Within a slow cluster, particles gradually become faster as the distance from center increases, as shown in Fig. 2 (e). Analogous pattern is also observed in a recent study [68]. When a start-up shear is applied, the local response is reflected by the distribution of τ_{sh} . According to the previous analysis, as $\dot{\gamma}$ increases, more particles will be involved as slow ones, manifested by the expansion of slow clusters. This trend is clearly seen in Fig. 4. Figure 4 (a) shows the spatial distribution of τ_{LC} for sample A at equilibrium. Figure 4 (b) – (d) show the spatial distributions of τ_{sh} of sample A under start-up

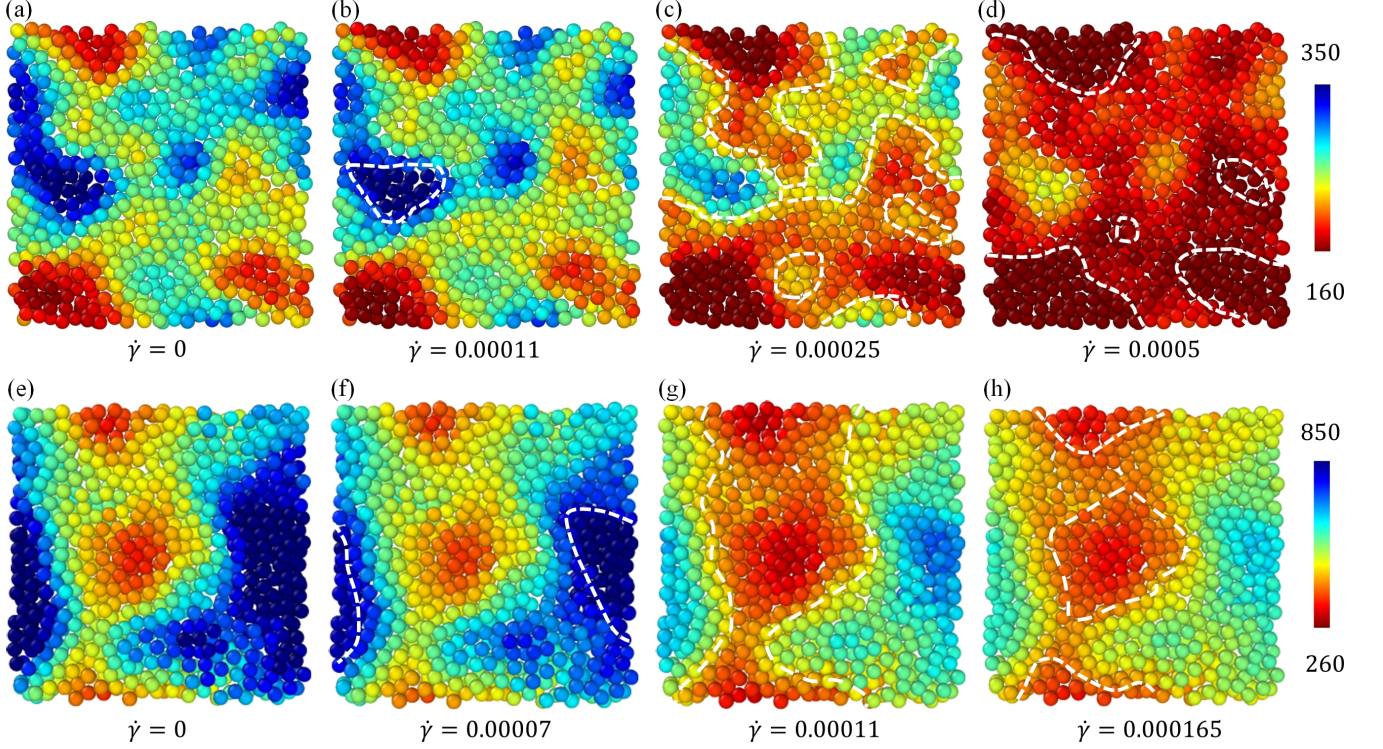


FIG. 4. (a) Slice of the spatial distribution of τ_{LC} of sample A at equilibrium. (b) – (d) Slices of the spatial distribution of τ_{sh} of sample A obtained under start-up shear with various $\dot{\gamma}$ denoted at each panel. In (b) – (d), white dashed lines denote the boundaries between fast and slow groups of particles found by Eq. 2. (e) – (h) show the results for sample B.

shear with various $\dot{\gamma}$. The boundaries of slow clusters, found by $\tau_{sh,b} = \tau_{LC,c} - \tau_2$, are denoted by dashed lines (the detailed method for circling these clusters is given in Appendix A). It is seen that τ_{LC} and τ_{sh} exhibit similar heterogeneous features. Moreover, the boundaries of slow clusters expand as $\dot{\gamma}$ increases. Same observation is found for sample B, as shown in Fig. 4 (e) – (h).

For the meaning of “slow” and “fast”, we would like to discuss the following two points. (i) As $\dot{\gamma}$ increases, the mean value of τ_{sh} decreases, suggesting faster dynamics. On the other hand, more particles are involved in slow regions. These two observations are not contradictory. When we identify a group of particles as slow, it means that their mobility is slower than external shear. Thus, as $\dot{\gamma}$ increases, the dynamics is facilitated by shear, meanwhile, more particles become slower than the external shear and are identified as slow ones. (ii) Considering that the spectra of τ_{sh} and τ_{LC} are not bimodal, one may feel that the dichotomy used here is too rough. Especially, for particles with mediate mobility, whether they are fast or slow is obscure. This problem can be clarified by the clustering feature of slow/fast regions. As discussed in the preceding paragraph, typically, a slow (or fast) cluster has a center formed by a few very slow (or fast) particles. As the distance from the center increases, particles gradually become faster (or slower). Consequently, the particles with mediate mobility are mainly at

the boundaries between fast and slow clusters. Whether they are identified as slow or fast may result in small fluctuation of the boundaries, but will not influence the identification of a cluster to be slow or fast.

The emergence of slow and fast clusters allows us to explore the heterogeneity in mechanical response. For each cluster, we calculate its shear stress by summing the atomic level stresses [69] of its constituent particles during the start-up process. Then, by averaging the results of all slow (or fast) clusters, we obtain the response of the slow (or fast) part. To mitigate the effect of thermal fluctuations, stresses are further averaged over ICE. In Fig. 5, we present the start-up shear stresses of slow part ((a) and (b)) and fast part ((c) and (d)) for both samples at different $\dot{\gamma}$. For clarity, the transient stress $\sigma(t)$ is scaled using the corresponding stable-state stress, ensuring that the resulting dimensionless stress $\sigma^*(t)$ is equal to 1 at long time. We find that the stress of slow part exhibits an overshoot, a feature typically observed in glasses [70, 71]. In contrast, the stress of fast part exhibits a smooth transition to stable state without a distinct overshoot. This behavior can be described by the Maxwell model as $\sigma^*(t) = 1 - \exp(-t/\tau_f)$, where τ_f is the Maxwell time of fast part. As $\dot{\gamma}$ increases, τ_f is seen to decrease, meaning that the fast part becomes faster and approaches ideal viscous liquid, corresponding to the shrinkage of fast regions with increasing $\dot{\gamma}$. This

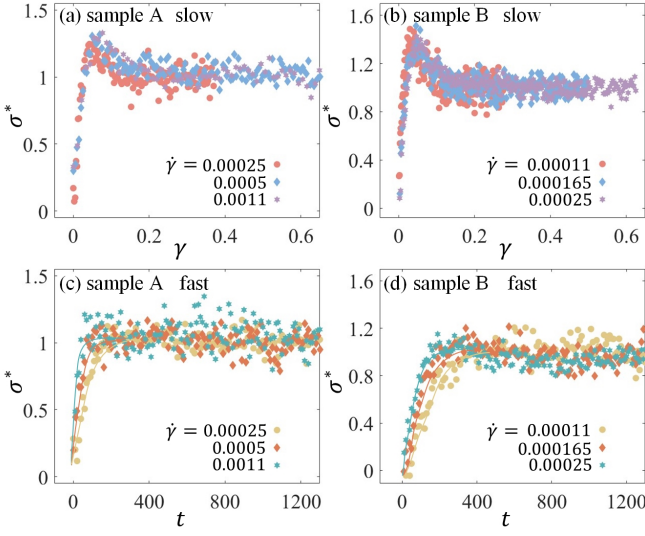


FIG. 5. (a) and (b) show the transient stresses of the slow part, normalized by the corresponding stable-state stresses, under start-up shear with various $\dot{\gamma}$ for sample A and sample B, respectively. In both (a) and (b), we adopt $\gamma = \dot{\gamma}t$ as the time variable. (c) and (d) show the transient stresses of the fast part, normalized by the corresponding stable-state stresses, under start-up shear with different $\dot{\gamma}$ for sample A and sample B, respectively. In both (c) and (d), lines denote the fits with $\sigma^*(t) = 1 - \exp(-t/\tau_f)$.

observation is consistent with our previous analysis given by Figs. 3 and 4. It should be pointed out that whether there is an overshoot is not a necessary and sufficient condition to distinguish between solid-like and liquid-like responses [70, 72]. Even so, the difference between the responses of slow and fast parts is unambiguous. In the next subsection, the coexistence of solid-like and liquid-like responses will be clearly revealed in the flow under steady shear.

C. τ_{LC} in flow and local response to steady shear

In the preceding subsection, we explore the connection between DH and local mechanical response to start-up shear through the concept of τ_{LC} . A key to this connection is the functional form of $\tau_{sh}(\tau_{LC})$, which determines whether a particle behaves slowly or fast in response to shear. Then, a natural question is raised: How can the insight derived from the start-up shear guides our understanding of other flow conditions? In this subsection, we will discuss the steady shear, the most common nonequilibrium condition in fluid study.

For a steady shear with $\dot{\gamma}$, we calculate its τ_{LC} with respect to a given time t_0 as follows: First, we switch off the shear flow at $t = t_0$, and measure the first-jump time from t_0 for every particle. Then, we perform the ICE average according to the configuration at $t = t_0$ with keeping the shear off from $t = t_0$. Besides τ_{LC} , we also

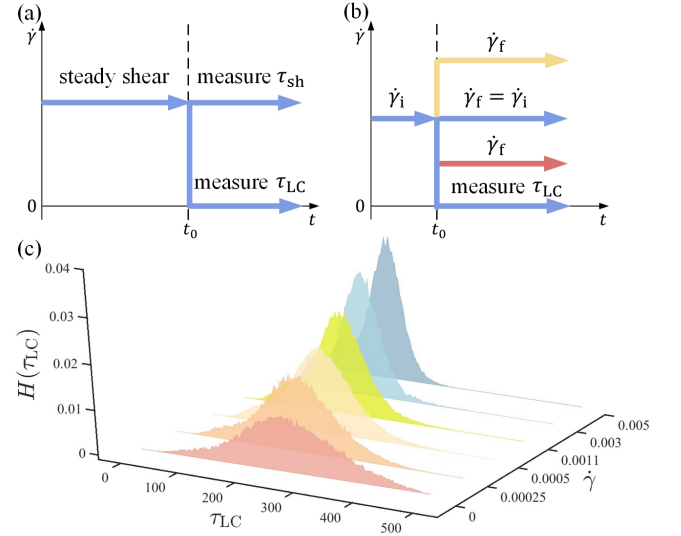


FIG. 6. (a) Schematic diagram for illustrating the flow conditions for measuring τ_{LC} and τ_{sh} under steady shear with respect to a configuration at time t_0 . (b) Schematic diagram for illustrating the flow conditions for testing the universality of $\tau_{sh}(\tau_{LC})$. Here, the shear rate is abruptly altered from the initial value $\dot{\gamma}_i$ to a final value $\dot{\gamma}_f$ at $t = t_0$. (c) Distributions of τ_{LC} ($H(\tau_{LC})$) at equilibrium and under steady shear with various $\dot{\gamma}$.

calculate the first-jump time from $t = t_0$ in shear flow τ_{sh} . In calculating τ_{sh} , the steady shear is kept on, and the ICE average is still employed. The flow conditions for calculating τ_{LC} and τ_{sh} are illustrated in Fig. 6 (a). In the study of polymer dynamics, the abrupt cessation of flow is widely used, and its relaxation time is intimately linked to the constitutive model [6, 73]. However, for most studies of flow behaviors of particulate liquids and glasses, characteristic relaxation times are measured in the continuous flow [43, 74–76]. The times characterizing the process after the cessation of flow, though appearing in a few studies [72, 77], have not attracted enough attention. Note that τ_{sh} is determined by the combined effect of the steady convection and the thermal activation from the configuration at $t = t_0$. In contrast, by switching off the shear, the steady convection is eliminated and, thus, τ_{LC} is mainly determined by the thermal activation from the distorted configuration at $t = t_0$. In Fig. 6 (c), we plot the distributions of τ_{LC} at equilibrium and under steady shear with various $\dot{\gamma}$ for sample A. The distribution of τ_{LC} shifts to lower values as $\dot{\gamma}$ increases, corresponding to more distorted configurations at larger $\dot{\gamma}$.

Figure 7 gives the $\tau_{sh}(\tau_{LC})$ relations in steady shear (symbols) for both samples at various $\dot{\gamma}$ covering both the crossover regime and the shear-thinning regime. In addition, we replot the results for the start-up shear that have been shown in Fig. 3 (a) and (b) (lines). It is noteworthy that the symbols well align with the line for each $\dot{\gamma}$. This nontrivial agreement suggests that the relation

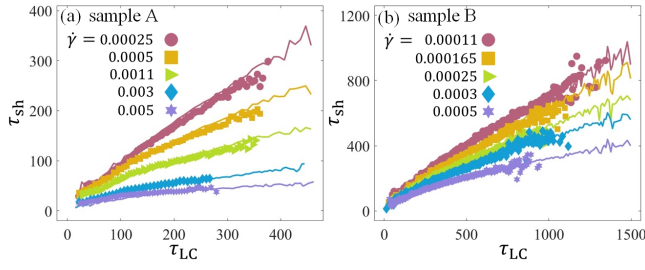


FIG. 7. (a) and (b) show $\tau_{sh}(\tau_{LC})$ obtained under steady shear (symbols) with various $\dot{\gamma}$ for sample A and sample B, respectively. In addition, the results shown in Fig. 3 (a) and (b), which are obtained by applying start-up shear, are replotted here by lines. Here, lines and symbols corresponding to the same $\dot{\gamma}$ are plotted in the same color.

between τ_{sh} and τ_{LC} is universal for a given $\dot{\gamma}$, irrespective of whether the flow is steady or start-up.

To examine the likely universality of the $\tau_{sh}(\tau_{LC})$ relation mentioned above, we conduct additional tests as follows. As illustrated in Fig. 6 (b), we first let the system be in a steady state with a shear rate $\dot{\gamma}_i$. Then, we perform an abrupt change of shear rate from $\dot{\gamma}_i$ to $\dot{\gamma}_f$ at $t = t_0$. Steady shear is just a special case where $\dot{\gamma}_f = \dot{\gamma}_i$. Both τ_{LC} and τ_{sh} with respect to $t = t_0$ are calculated. In Fig. 8 (a), we show the results of $\tau_{sh}(\tau_{LC})$ with $\dot{\gamma}_f = 0.0011$ and several $\dot{\gamma}_i$ ranging from $\dot{\gamma}_i = 0$ to $\dot{\gamma}_i = 0.003$ for sample A. Notice that, the conditions here include both $\dot{\gamma}_i < \dot{\gamma}_f$ and $\dot{\gamma}_i \geq \dot{\gamma}_f$. It is seen that the $\tau_{sh}(\tau_{LC})$ relations at different $\dot{\gamma}_i$ remarkably coincide for the same $\dot{\gamma}_f$. Such coincidence is also found for different $\dot{\gamma}_f$ (Fig. 8 (b)) and different samples (Fig. 8 (c) and (d)). The results shown in Figs. 7 and 8 suggest that the functional form of $\tau_{sh}(\tau_{LC})$ is universal once the final shear rate $\dot{\gamma}_f$ is given. This observation implies that the transient configuration (i.e., the configuration at $t = t_0$, determined by the initial shear rate $\dot{\gamma}_i$) and the convective effect (determined by $\dot{\gamma}_f$) independently contribute to the local relaxation.

In Fig. 4, we show that the heterogeneous patterns of τ_{LC} and τ_{sh} are highly alike for the start-up shear. This likeness is also found in all other flow conditions. An example for steady shear is shown in Fig. 9. The similarity between the DH patterns of τ_{LC} and τ_{sh} , together with the universal form of $\tau_{sh}(\tau_{LC})$ relation shown in Fig. 7 and 8, suggest an approximate one-to-one correspondence between τ_{LC} and τ_{sh} . It is interesting to note that in steady-shear cases, τ_{LC} is a hidden parameter because it is not directly measurable in the continuous flow. To find τ_{LC} , one has to switch off the shear, which is incompatible with the condition of steady shear. On the other hand, τ_{sh} can be measured directly in the flow. With the one-to-one correspondence between τ_{LC} and τ_{sh} , we can obtain the hidden τ_{LC} once the distribution of τ_{sh} is known.

Knowing the approximate one-to-one correspondence between τ_{LC} and τ_{sh} in flow, we conjecture that the local

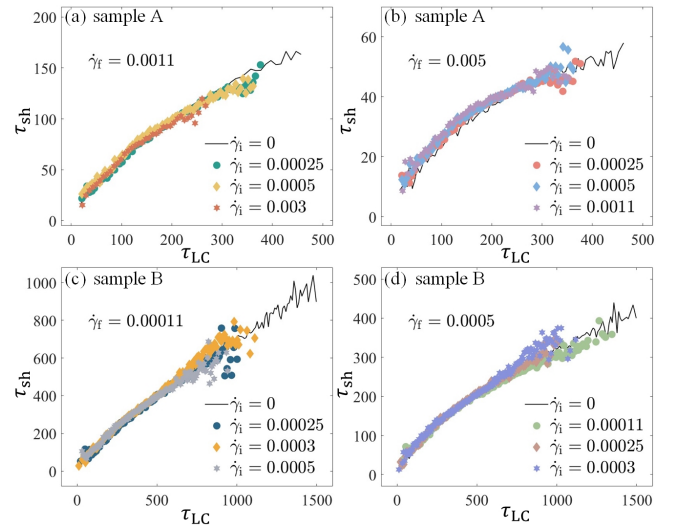


FIG. 8. Demonstration of the universality of the $\tau_{sh}(\tau_{LC})$ relation with respect to $\dot{\gamma}_f$. (a) shows the $\tau_{sh}(\tau_{LC})$ relations obtained with $\dot{\gamma}_f = 0.0011$ and various $\dot{\gamma}_i$ for sample A. (b) shows the results for another given final shear rate $\dot{\gamma}_f = 0.005$ for sample A. (c) and (d) display the results for sample B. In all panels, the results of $\tau_{sh}(\tau_{LC})$ with different $\dot{\gamma}_i$ collapse for a given $\dot{\gamma}_f$.

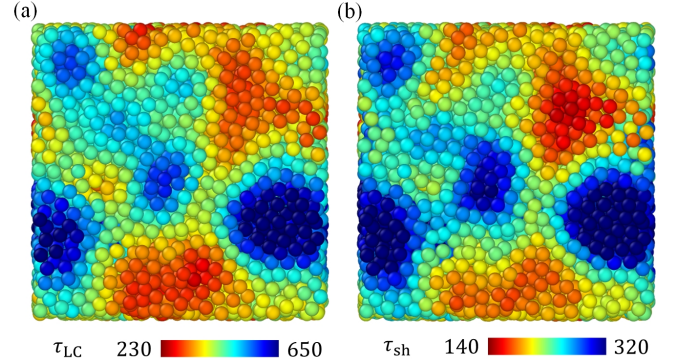


FIG. 9. Snapshots of the slice of the spatial distribution of τ_{LC} (a) and τ_{sh} (b) for sample B under steady shear with $\dot{\gamma} = 0.0003$.

mechanical response, which should be closely related to τ_{sh} , exhibits spatial heterogeneity with a pattern similar to that of τ_{LC} . As to the heterogeneity in response, we proposed a concept of localized elastic region (LER) [42] recently, inspired by the idea of “solidity” in supercooled liquids [78–82]. An LER, typically composed of hundreds of particles, is a transient, solid-like cluster capable of accumulating elastic stress in the flow of supercooled liquid. Under the steady shear, especially in the nonlinear regime, the generation, deformation and relaxation of LER are ubiquitous and successive [42, 83], contributing to the viscoelasticity of supercooled liquids. The existence of LER signifies the heterogeneity in the local response to shear: some regions behave elastically, while

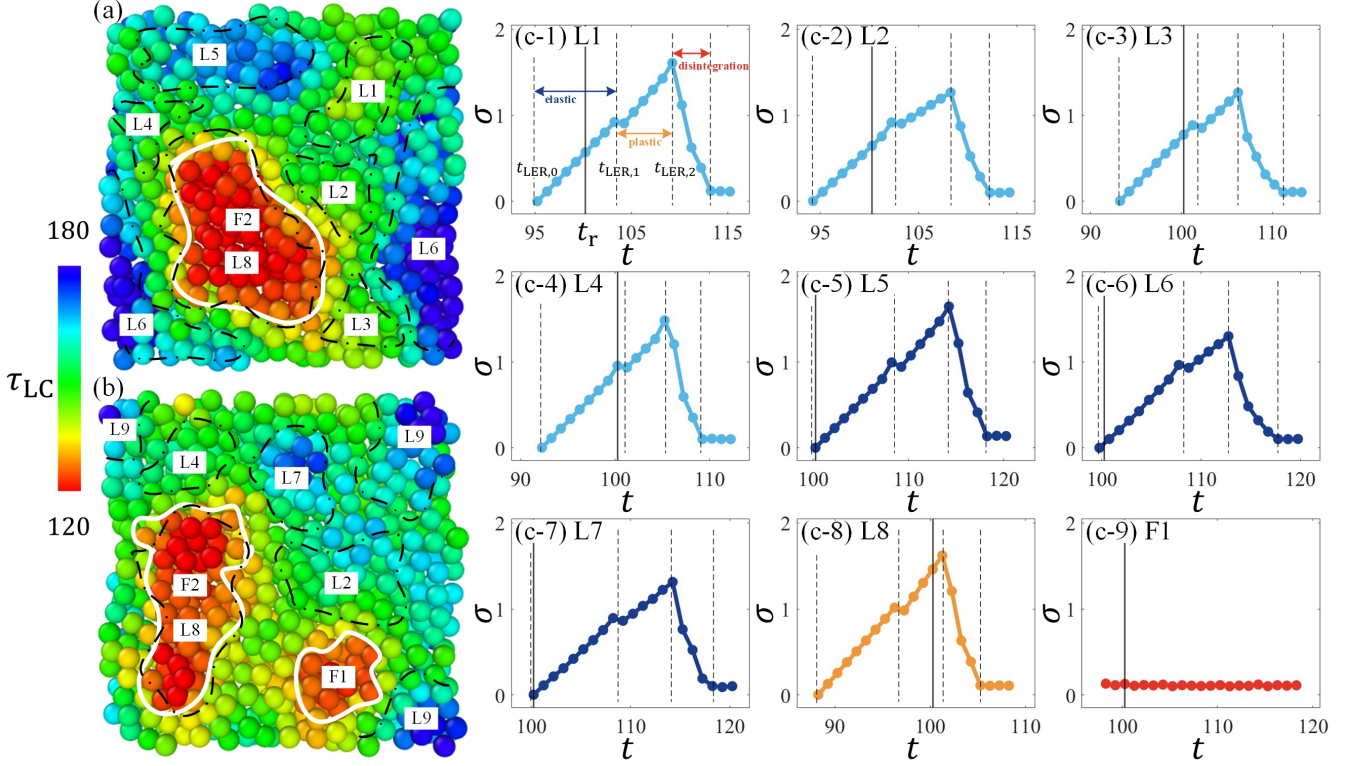


FIG. 10. DH and heterogeneity in local response under steady shear. (a) and (b) show two slices of the spatial distribution of τ_{LC} of sample A under steady state with $\dot{\gamma} = 0.003$ at a reference time t_r . Nine LERs are found at $t = t_r$. We label them with L1, L2, ..., L9, and denote their boundaries by black dash-dot lines. The boundaries of slow and fast groups are denoted by white solid lines. There are two fast clusters within these two slices, and are labeled with F1 and F2. In (c-1) - (c-8), we respectively show the evolution of the stress sustained by the LER for L1 - L8. In each panel, we use vertical dashed lines to demarcate the three stages, namely, elastic deformation, plastic yielding, and disintegration, as illustrated in (c-1). In (c-9), we show the evolution of the stress of the fast cluster F1. In (c-1) - (c-9), vertical solid lines are used to denote the reference time t_r .

other regions behave as viscous liquid. Then a question arises naturally: Does LER correlate with the heterogeneous distribution of τ_{LC} and the grouping of fast and slow particles? Figure 10 (a) and (b) show two slices of system A under the steady shear with $\dot{\gamma} = 0.003$ at a reference time denoted as t_r . The color of each particle denotes its value of τ_{LC} measured at $t = t_r$. With the method given in Ref. [83], we identify nine LERs in the system at $t = t_r$. In Fig. 10 (a) and (b), we denote their boundaries with black dash-dot lines, and label them with L1, L2, ..., L9. Meanwhile, we also plot the boundaries between the fast and slow groups determined by Eq. 2 with white solid lines. Two distinct fast clusters are found within these two slices, and are labeled with F1 and F2 in Fig. 10 (a) and (b). In Fig. 10 (c-1) - (c-8), we plot the evolution of the stresses sustained by LERs L1 - L8 (the stress of L9 is not shown due to the limited space of Fig. 10). It is seen that an LER sequentially undergoes elastic deformation, plastic yielding, and sharp disintegration that eventually transforms it into a liquid-like state [83]. An example of these three stages is denoted in Fig. 10 (c-1): Here, the beginnings of elas-

tic deformation, plastic yielding, and disintegration are denoted as $t_{LER,0}$, $t_{LER,1}$, and $t_{LER,2}$, respectively. In our recent work [83], we have shown that the appearance of plasticity at $t = t_{LER,1}$ is accompanied by the emergence of cage-jump spots, where cage jumps highly concentrate within a few diameters of particle, inside the LER. By calculating the pseudoharmonic modes [84], we show that [83] these soft spots constitute the manifestation of the shear transformation zones (STZ) [85-88]. This is very similar to amorphous solids, where STZs play as the precursor of the mechanical failure. In Fig. 10 (c-9), we show the stress evolution of the fast cluster labeled with F1. No stress accumulation is seen here. The stress is steady, similar to the macroscopic behavior of viscous liquids under steady shear.

In the system, LERs are in different stages at a given time. To clarify the stages of the LERs at $t = t_r$, we denote the reference time t_r by vertical solid lines in Fig. 10 (c-1) - (c-8). As seen in Fig. 10 (c-1) - (c-7), for LERs L1 - L7 (and L9, not shown in Fig. 10), the corresponding LER is in the elastic deformation stage (i.e., within the period of $[t_{LER,0}, t_{LER,1}]$). In contrast, for LER L8, as

seen from Fig. 10 (c-8), it is in the plastic yielding stage (i.e., within the period of $[t_{\text{LER},1}, t_{\text{LER},2}]$), and is very close to the disintegration. By examining Fig. 10, we find following correlation between LER and the spatial distribution of τ_{LC} :

(i) For slow particles, most of them are involved in the elastic deformation stage of LER. Their atomic level stresses will continue to build up until the yielding of LER. This point is manifested by the observation that the slow region highly overlaps with the regions occupied by LERs L1 – L7 and L9, for which the reference time t_r is within the elastic stages of these LERs. By checking several flow conditions, we find that there are nearly 80% of slow particles are involved in the elastic deformation stage of LER.

(ii) For fast particles, there are two situations. One is exemplified by the fast cluster F1. It is out of all LERs. As shown in Fig. 10 (c-9), it behaves as a typical viscous liquid. The other one is exemplified by the fast cluster F2. In space, it nearly coincides with the LER L8, which is very close to its disintegration at $t = t_r$ as shown in Fig. 10 (c-8). This coincidence is understandable, since the imminent disintegration of LER involves strong displacements of most of its constituent particles [83]. In either case, the stress of the fast cluster cannot accumulate.

Summarizing the results shown in Fig. 10, we conclude that under steady shear, the regions composed of slow particles exhibit elastic response to imposed shear, while the fast regions behave as viscous liquid. In this way, we establish a correlation between DH and local mechanical response.

D. Functional form of $\tau_{\text{sh}}(\tau_{\text{LC}})$

The functional form of $\tau_{\text{sh}}(\tau_{\text{LC}})$ plays a critical role in the above discussion. In fact, for all cases studied in this work, $\tau_{\text{sh}}(\tau_{\text{LC}})$ can be nicely fitted by an exponential form:

$$\tau_{\text{sh}} = \tau_{\text{sh}}^{\infty} \left[1 - \exp\left(-\frac{\tau_{\text{LC}}}{\tau_0}\right) \right], \quad (3)$$

where $\tau_{\text{sh}}^{\infty}$ and τ_0 are fitting parameters. τ_0 governs the position at which $\tau_{\text{sh}}(\tau_{\text{LC}})$ significantly deviates from $\tau_{\text{sh}} = \tau_{\text{LC}}$. It reflects the time scale of the external shear. Thus, we expect that τ_0 depends on $\dot{\gamma}^{-1}$ linearly. Figure 11 (a) and (b) give the fitted τ_0 as a function of $\dot{\gamma}^{-1}$ for sample A and sample B, respectively, from where the linearity is clearly seen. $\tau_{\text{sh}}^{\infty}$ represents the dynamics of the slowest particles in the flow. These particles, according to our above analysis, are mostly involved in LERs. We can define the characteristic strain for these particles by $\gamma_{\text{sh}}^{\infty} = \dot{\gamma} \tau_{\text{sh}}^{\infty}$. In Ref. [42], it is demonstrated that in the shear-thinning regime, the strain of LER γ_{LER} varies with $\dot{\gamma}$ by $\gamma_{\text{LER}} \sim \dot{\gamma}^{\epsilon}$ with $\epsilon = 1 - \lambda$. Therefore, we expect $\gamma_{\text{sh}}^{\infty} \sim \dot{\gamma}^{\epsilon}$, or equivalently, $\tau_{\text{sh}}^{\infty} \sim \dot{\gamma}^{-\lambda}$. The fitted $\tau_{\text{sh}}^{\infty}$ as a function of $\dot{\gamma}$ are plotted in log-log scale

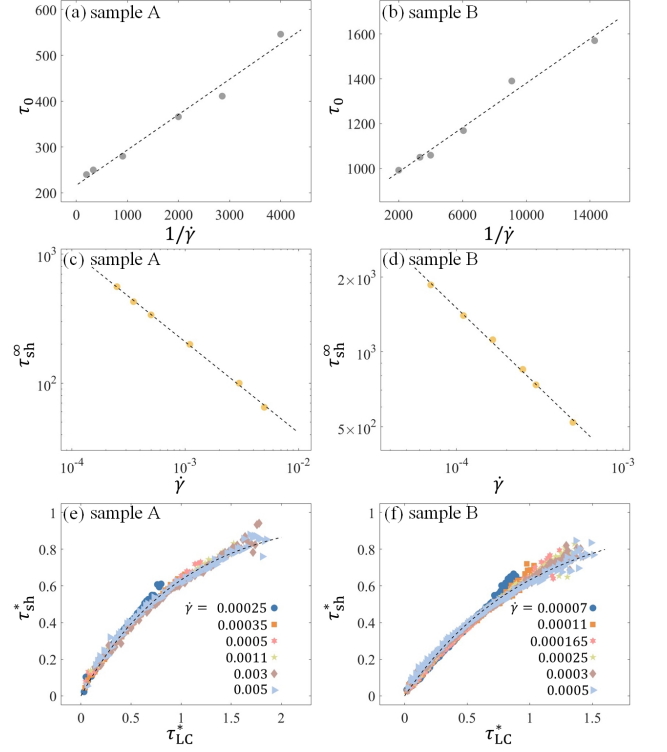


FIG. 11. (a) and (b) show the fitted τ_0 as a function of $\dot{\gamma}^{-1}$ for sample A and sample B, respectively. Dashed lines in (a) and (b) denote the linear relation between τ_0 and $\dot{\gamma}^{-1}$. (c) and (d) show the fitted $\tau_{\text{sh}}^{\infty}$ as a function of $\dot{\gamma}$ for sample A and sample B, respectively. Dashed lines in (c) and (d) denote the relation of $\tau_{\text{sh}}^{\infty} \sim \dot{\gamma}^{-\lambda_{\tau}}$. (e) and (f) give the rescaled relations of $\tau_{\text{sh}}(\tau_{\text{LC}})$, denoted as $\tau_{\text{sh}}^*(\tau_{\text{LC}}^*)$, for sample A and sample B, respectively. Dashed lines in (e) and (f) represent the master curves given by Eq. 4.

for both samples in Fig. 11 (c) and (d). The relation of $\tau_{\text{sh}}^{\infty}(\dot{\gamma})$ indeed exhibits a power-law dependence, denoted as $\tau_{\text{sh}}^{\infty} \sim \dot{\gamma}^{-\lambda_{\tau}}$. The fitted value of the power λ_{τ} is 0.70 for sample A, and 0.65 for sample B. As we expect, these values are very close to the corresponding λ . Note that the power law of $\tau_{\text{sh}}^{\infty} \sim \dot{\gamma}^{-\lambda_{\tau}}$ covers the whole range of $\dot{\gamma}$ studied in this work, and is not limited to the shear-thinning regime. According to these considerations, we can rescale τ_{sh} as $\tau_{\text{sh}}^* = \tau_{\text{sh}}/(c\dot{\gamma}^{-\lambda})$, and rescale τ_{LC} as $\tau_{\text{LC}}^* = \tau_{\text{LC}}/(a\dot{\gamma}^{-1} + b)$, where a , b and c are material-dependent parameters. Then, Eq. 3 is rewritten as

$$\tau_{\text{sh}}^* = 1 - \exp(-\tau_{\text{LC}}^*). \quad (4)$$

We rescale our data found from different conditions with the above method for both samples, and show the results in Fig. 11 (e) and (f). All data well collapse onto the master curve given by Eq. 4. Note that, since the exponent λ is involved in this rescaling, Eq. 4 implies an intrinsic relation between the nonlinear rheology of the system and the interplay between convection and thermal activation.

Here, both the values of λ of two samples are close to 2/3. Similar results are also observed in other LJ super-

cooled liquids in a wide range of supercooled temperatures [89]. Moreover, for Brownian dynamics simulations of supercooled charged colloids with hard-sphere Yukawa interaction, it is found that λ ranges from 0.64 to 0.7, which are also closely around $2/3$ [42]. In fact, $2/3$ is the prediction of a mean-field theory [90]. Therefore, by assuming $\tau_{\text{sh}}^\infty = c\dot{\gamma}^{-2/3}$, the obtained τ_{sh}^∞ still effectively rescale the data of $\tau_{\text{sh}}(\tau_{\text{LC}})$ onto Eq. 4.

We will get back to the form of $\tau_{\text{sh}}(\tau_{\text{LC}})$ in Sec. V.

III. SOLID-LIQUID DUALITY AND RHEOLOGY

In the preceding section, we establish the correlation between DH and local mechanical response to imposed shear in supercooled liquids. It is found that the way of local response highly depends on the comparison between the local mobility, represented by τ_{LC} , and the time scale of external shear, which linearly depends on $\dot{\gamma}^{-1}$. Though the spectrum of τ_{LC} is smooth, the local response exhibits two major ways: solid-like for slow particles, and liquid-like for fast particles. This solid-liquid duality in response can be viewed as a specific implementation of Maxwell's insight into viscoelasticity at the microscopic level. Additionally, it is crucial to note that slow/fast particles do not randomly distribute through the system. Instead, they tend to aggregate into clusters. With this picture, we will explore the microscopic mechanisms of two important rheological behaviors for supercooled liquids, namely, steady shear and start-up shear, in this section.

A. Rearrangements of solid-like and liquid-like regions

To employ the microscopic solid-liquid duality, it is important to clarify the difference between the rearrangements of solid-like and liquid-like regions first. Figure 12 (a) and (b) display the stress evolutions of a solid-like region (the LER L5 in Fig. 10) and a liquid-like region (the fast cluster F1 in Fig. 10) in simple A, respectively. For each region, we calculate the ratio of constituent particles that have undergone cage jump since $t = t_{\text{in}}$, denoted as $R_{\text{cj}}(t)$. Here, t_{in} , marked in Fig. 12 (a) and (b), is the beginning time of the elastic deformation of LER L5. The results of $R_{\text{cj}}(t)$ are shown in Fig. 12 (c) and (d). As seen from Fig. 12 (c), for the solid-like region, $R_{\text{cj}}(t)$ increases slowly in the elastic deformation stage, and then grows much more rapidly as the cluster enters the plastic yielding process. In contrast, $R_{\text{cj}}(t)$ for the liquid-like region increases in a nearly linear form, as shown in Fig. 12 (d). The difference between Fig. 12 (c) and (d) reflect that solid-like region and liquid-like region rearrange in fundamentally different ways, as we will discuss in following two paragraphs.

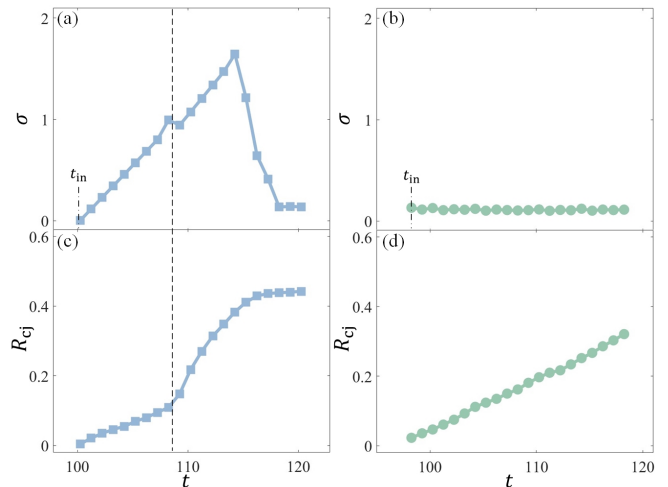


FIG. 12. (a) and (b) reproduce the stress evolutions of the LER L5 (representing a solid-like region) and the fast cluster F1 (representing a liquid-like region) in Fig. 10. t_{in} is the time at which the LER L5 starts to accumulate elastic stress. (c) and (d) give the jump ratio $R_{\text{cj}}(t)$ for the above two regions. In (a) and (c), we denote the end of elastic deformation stage by a vertical dashed line.

For liquid-like regions, the linear form of $R_{\text{cj}}(t)$ suggests that cage jumps take place independently. This result is consistent with Ref. [91], which demonstrates that the phonon propagation induced by a cage jump in normal liquids is highly localized and short-lived. In this case, due to the absence of the long-ranged elasticity-mediated interaction, most cage jumps cannot be correlated and, thus, are activated independently.

For solid-like regions, $R_{\text{cj}}(t)$ exhibits an evident crossover at the end of the elastic deformation stage. To understand this nontrivial phenomenon, we recall that the yielding process of amorphous solids is collective and hierarchical [59], where the facilitation due to the long-ranged anisotropic elasticity-mediated interaction plays a crucial role [92–94]. Particularly, when only a small fraction of particles undergo rearrangements, the system remarkably loses its ability to further accumulate elastic stress: As suggested in Ref. [95], the failure of amorphous solids occurs when only about 10% of particles are involved in STZs. As for LER, its response is very similar to that of amorphous solids, as shown in Fig. 10 and Ref. [83]. Especially, the end of its elastic deformation is accompanied by the emergence of cage-jump spots that manifest STZs [83]. With these considerations, the observation shown in Fig. 12 (c) is understandable: During the elastic deformation stage of LER, cage jumps are relatively rare, and $R_{\text{cj}}(t)$ grows slowly with t . As $R_{\text{cj}}(t)$ exceeds about 10%, the elasticity cannot be well sustained any longer. Then, plastic yielding and disintegration successively occur, accompanied by overwhelming cage jumps that result in the rapid growth of $R_{\text{cj}}(t)$.

B. Steady shear

Under steady shear, both samples exhibit shear thinning, as shown in Fig. 1. It can be described by a phenomenological expression $\eta(\dot{\gamma}) \approx \eta_{\text{eq}} / [1 + (\tau_{\eta} \dot{\gamma})^\lambda]$, where η_{eq} is the zero-shear viscosity, and τ_{η} is a parameter with the dimension of time [2, 43, 96]. As $\dot{\gamma}$ increases from null, η gradually deviates from η_{eq} and finally behaves with a power law $\eta(\dot{\gamma}) \sim \dot{\gamma}^{-\lambda}$. To understand this complicated nonlinear behavior, we employ the solid-liquid duality by expressing the shear stress σ as:

$$\sigma(\dot{\gamma}) = \frac{1}{2} p_{\text{slow}} G_{\text{eff}} \dot{\gamma} \tau_{\text{el}} + (1 - p_{\text{slow}}) \eta_{\text{eq}} \frac{\bar{\tau}_{\text{sh,fast}}}{\bar{\tau}_{\text{LC,eq}}} \dot{\gamma}, \quad (5)$$

where the first term in the right-hand side of Eq. 5 represents the contribution from slow particles, and the second term represents the contribution from fast particles. We discuss the former first. p_{slow} is the fraction of slow particles. As demonstrated in Sec. IIC, most slow particles are involved in the elastic stage of LERs. Thus, this contribution is given by the average elastic stress of LER. Here, G_{eff} is the effective shear modulus of LER, and τ_{el} is the average time of duration of the elastic deformation of LER. In flow, an LER undergoes elastic loading, and then a sharp disintegration to unload. The factor 1/2 accounts for the averaging effect of this saw-tooth-like loading-unloading process.

τ_{el} and G_{eff} are needed to quantify the contribution from slow particles. τ_{el} is evaluated as follows. As we discuss in the preceding subsection, the end of the elastic deformation stage of an LER is accompanied by the cage jumps of about 10% of its constituent particles. Therefore, we determine τ_{el} as the waiting time that 10% of slow particles have relaxed according to the spectrum of τ_{sh} .

We now turn our attention to the effective modulus of LER G_{eff} . By “effective”, we mean that it encapsulates both elastic and plastic effects [71, 97]. To be specific, even in the elastic stage of LER, small amount of nonaffine displacements of constituent particles take place, as shown in Fig. 12 (c) and Ref. [83]. This plasticity slightly weakens the modulus of LER. Therefore, the modulus during the elastic stage can be written as $G_{\text{eff}} = w G_{\text{ini}}$, where G_{ini} is the initial shear modulus of LER, and w ($w < 1$) is a weakening factor reflecting this plasticity. To estimate w , we adopt a strategy that ties the variation in shear modulus to the neighbor loss process [71, 97]. The detail for calculating w and G_{eff} is given in Appendix B. For all studied conditions, we find that $G_{\text{eff}} \approx 0.8 G_{\text{ini}}$.

For fast particles, as we show in Fig. 10, they do not exhibit elastic deformation. Instead, such regions behave like viscous liquids. Considering that the average persistence time is found to be proportional to viscosity [62], we can estimate the viscosity of fast particles η_{fast} by the relation:

$$\frac{\eta_{\text{fast}}}{\eta_{\text{eq}}} = \frac{\bar{\tau}_{\text{sh,fast}}}{\bar{\tau}_{\text{LC,eq}}}, \quad (6)$$

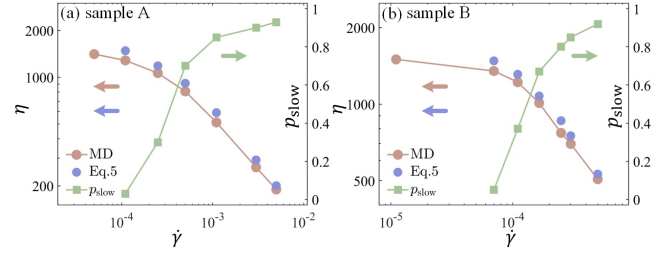


FIG. 13. In both (a) (representing sample A) and (b) (representing sample B), the viscosity estimated by Eq. 5, the viscosity directly measured from MD data, and the proportion of slow particles p_{slow} are given.

where $\bar{\tau}_{\text{LC,eq}}$ is the average of τ_{LC} at equilibrium, and $\bar{\tau}_{\text{sh,fast}}$ is the average of τ_{sh} of fast particles at the given shear rate. Here, $\bar{\tau}_{\text{sh}}$ can be approximated by $\bar{\tau}_{\text{LC}}$ for fast particles. With Eq. 6, we obtain the second term in the right-hand side of Eq. 5.

Figure 13 shows the results of viscosity calculated by Eq. 5 for two samples. The accurate results, shown in Fig. 1, are replotted here for comparison. The agreement between two results is remarkable. We also show the results of p_{slow} in Fig. 13. It is seen that p_{slow} is negligible at the Newtonian regime. As $\dot{\gamma}$ increases, p_{slow} becomes finite, meanwhile, noticeable shear thinning appears. As $\dot{\gamma}$ further increases, p_{slow} grows rapidly, and then saturates in the shear thinning regime. These observations clearly reveal the relation between DH and the onset of shear thinning: Due to the heterogeneous dynamics, different regions in a supercooled liquid respond to shear in different ways. Slow particles tend to aggregate into LERs. The accumulation of elastic stress and strain of LER, which is limited by thermal activation and shear-driven effects, cannot catch up with the growth of $\dot{\gamma}$. Thus, the viscosity contributed by slow particles shear-thins. As $\dot{\gamma}$ becomes larger, more particles are involved as slow particles, results in progressively prominent shear thinning. When $\dot{\gamma}$ is very large, most particles are involved in LERs. Consequently, the nonlinear rheology of the system, described by $\eta \propto \dot{\gamma}^{-\lambda}$, is dominated by the behavior of LER. As we demonstrate in Ref. [42], in the shear-thinning regime, the characteristic length ξ_{LER} and strain γ_{LER} of LER, respectively, depend on $\dot{\gamma}$ by $\xi_{\text{LER}} \propto \dot{\gamma}^{-v}$ and $\gamma_{\text{LER}} \propto \dot{\gamma}^{\epsilon}$. Then, the exponent λ is determined by LER through the scaling relation $\lambda = 4v = 1 - \epsilon$.

It is worth noting that the onset of noticeable thinning takes place at a shear rate much smaller than τ_{α}^{-1} [43, 98, 99], where τ_{α} is the equilibrium α relaxation time [10]. The origin of this observation has been much debated. Particularly, the mode-coupling-theory (MCT) approach predicts that this onset shear rate is close to τ_{α}^{-1} [100–102]. It should be noted that the MCT approach highlights the caging effect and advection, while it does not explicitly involve DH. Within our framework, the aforementioned observation is easy to understand.

Owing to DH, there are regions with relaxation times much longer than τ_α . Such slow regions can be accelerated by shear at a shear rate much smaller than τ_α^{-1} , which leads to the emergence of shear thinning.

C. Start-up shear

The success shown in Fig. 13 implies that the particle-level solid-liquid duality provides a potential scenario for understanding the flow of supercooled liquids. With above considerations, now we explore the response of supercooled liquids to the start-up shear. Our objective is to predict the stress evolution during the start-up process with the knowledge of the equilibrium state, such as the equilibrium spectrum of τ_{LC} . The form of $\tau_{sh}(\tau_{LC})$ is crucial here. As we discussed in Sec. IID, for a specific sample, the form of $\tau_{sh}(\tau_{LC})$ is given by Eq. 4 once a few material-dependent parameters are known. Note that for the study of amorphous solids, the deformation and plastic yielding in the start-up process are of central importance [86, 103]. However, studies focusing on the start-up process of supercooled liquids are much less. While some research [104] has identified the shear banding phenomenon in supercooled liquids under high shear rates, a more general understanding remains elusive.

Recently, the progress in the elastoplastic model (EPM) significantly advances the quantitative understanding of the start-up behavior of glass [92, 105–107]. In this approach, a glass is discretized into mesoscopic grid cells in space. Each grid cell is assigned an initial stress. Under external shear, these grid cells undergo stress variations over time, which can be described in terms of cyclic behavior. The elementary cycle of a grid cell includes three stages: elastic deformation, plastic yielding, and restructuring for the next loading cycle. During the restructuring stage, the grid cell redistributes its accumulated stress through the long-ranged anisotropic elasticity-mediated interaction crossing the system [92, 108].

Borrowing some ideas from EPM, we construct a simple model for supercooled liquids under shear. We still assume that the system is separated into many cells. Nevertheless, there is a key difference between our model and EPM: In our model, the inter-cell elasticity-mediated interaction is not present, and cells are independent of each other. To understand this setting, we recall that in supercooled liquids, LERs are localized, and are separated by liquid-like regions [42, 83]. In this case, phonons can only propagate within LER, while are quickly damped in liquid-like regions [91]. Therefore, if we assume that a cell conceptually corresponds to an LER or a liquid-like region (see Fig. 14 (a) for an illustration), it will be unnecessary to consider the elasticity-mediated interaction between cells. Consequently, we assume that each cell evolves independently. Notice that in supercooled liquids, it is suggested that the relaxations of different dynamic regions are also coupled [109, 110]. To describe

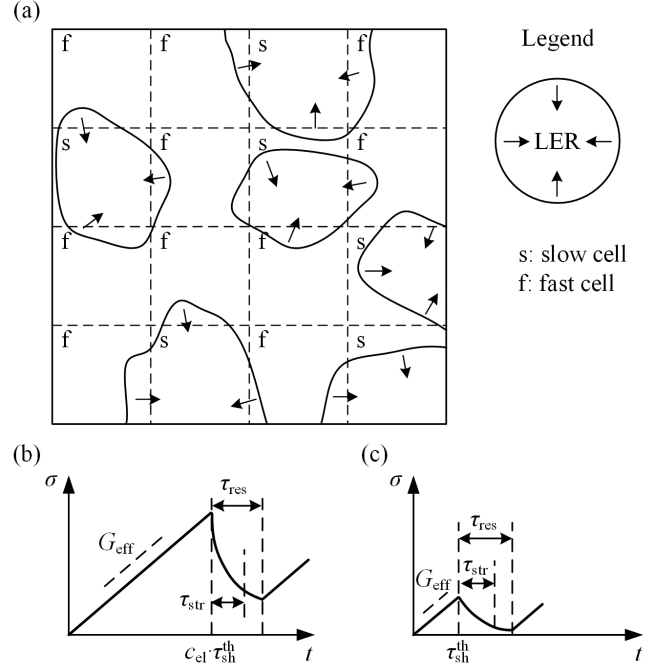


FIG. 14. (a) Schematic plot for illustrating the grid cell model of the flow of supercooled liquid. Conceptually, the system is divided into many cells. Since the system contains both slow and fast particles, each cell is classified as either slow (labeled as “s”) or fast (labeled as “f”). According to our analysis, LERs, represented by the curves, are expected to be predominantly composed of slow particles. In slow cells, phonons can propagate (as indicated by the arrows); otherwise, their propagation is damped. (b) One stress cycle of a slow cell. (c) One stress cycle of a fast cell.

this effect, a coupling factor can be introduced [110]. At the current stage, we ignore this effect to keep the model as simple as possible.

As shown in Fig. 2, the spatial distribution of τ_{LC} is smooth and tends to cluster in space. Thus, we can assign an average τ_{LC} value to each cell. In the beginning of the shear, we sample the average τ_{LC} value for each cell according to the equilibrium spectrum of τ_{LC} ($H_{eq}(\tau_{LC})$). Then, cells can be identified as fast or slow according to Eq. 2.

Recall that τ_{LC} is obtained with ICE, where the thermal fluctuation is eliminated. In other words, τ_{LC} should be regarded as the thermal-average jump time for a particle. In the presence of thermal fluctuation, we suggest that the actual jump time, τ_{LC}^{th} , follows a distribution with τ_{LC} being the mean, which is given by:

$$p_{th}(\tau_{LC}^{th}) = \frac{1}{\tau_{LC}} \exp\left(-\frac{\tau_{LC}^{th}}{\tau_{LC}}\right), \quad (7)$$

To account for this thermal effect, after assigning each cell a τ_{LC} sampled from $H_{eq}(\tau_{LC})$, we use the preceding distribution to sample τ_{LC}^{th} for each cell. With τ_{LC}^{th} , the local dynamics under shear, represented by τ_{sh}^{th} , can be

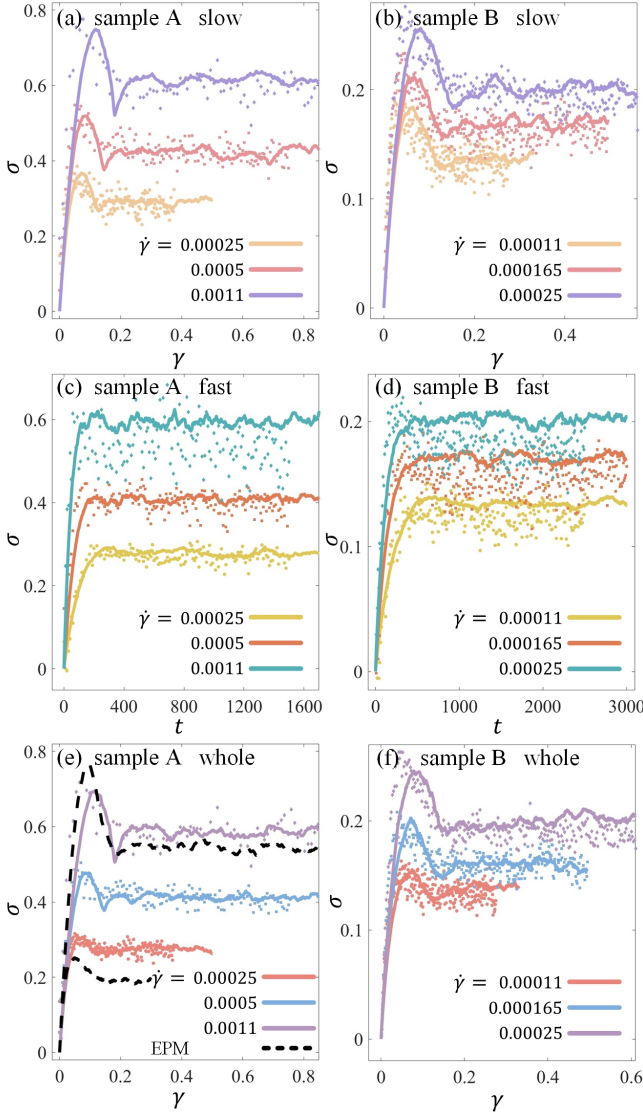


FIG. 15. Stress responses of both samples during the start-up process with several $\dot{\gamma}$. (a) and (b) respectively show the results of slow particles in sample A and sample B. (c) and (d) respectively show the results of fast particles in sample A and sample B. Note that, “slow” and “fast” denote the classification at the beginning of shear. (e) and (f) respectively show the results of the whole system for sample A and sample B. In all panels, symbols denote the MD results, and solid lines denote the results predicted by our model. In (e), black dashed lines denote the results calculated by the EPM approach. For the results of slow particles and the whole system, we adopt $\gamma = \dot{\gamma}t$ as the time variable.

found through Eq. 4.

Now we discuss the evolution of cell. Slow cells behave as solid and can be viewed as LERs. As we discuss in Sec. III A, the yielding and rearrangement of LER are collective due to the existence of the elasticity-mediated interaction. To embody this consideration in modeling, we recall our calculation in the preceding subsection: We use τ_{el} as the duration time of the elastic stage of LER,

rather than the average of τ_{sh} of slow particles $\bar{\tau}_{sh,slow}$. τ_{el} is noticeably shorter than $\bar{\tau}_{sh,slow}$. τ_{el} corresponds to the waiting time for about 10% of slow particles to relax. In contrast, $\bar{\tau}_{sh,slow}$ represents the time at which nearly half of slow particles have relaxed. For such a long time, the slow region has long lost its elasticity. To capture this effect, we introduce the ratio c_{el} :

$$c_{el} = \tau_{el} / \bar{\tau}_{sh,slow}. \quad (8)$$

Then, for a slow cell whose dynamics under shear is characterized by τ_{sh}^{th} , its duration of elasticity can be written as $c_{el} \tau_{sh}^{th}$.

The slow cell starts to yield after the elastic stage. Drawing upon the EPM framework [105], we employ an exponential form for the stress decrease during the unloading as $\sigma \sim \exp(-t/t_{str})$, where t_{str} represents a ballistic timescale. t_{str} is estimated by particle’s mean-square displacement (MSD) data prior to the onset of plateau behavior. For the sake of simplicity, we assume a constant t_{str} for all shear rates. Throughout this unloading stage, the cell is restructuring and preparing for the ensuing loading. Following Ref. [111], we introduce a restructuring strain γ_{res} . Given a shear rate $\dot{\gamma}$, the restructuring time τ_{res} is modeled as an exponentially distributed random variable with the mean given by $\gamma_{res}/\dot{\gamma}$. Figure 14 (b) illustrates a cycle of a slow cell.

In fast cells, the elasticity spanning an extended spatial region is not present. Cage jump is highly independent, in the sense that the phonon propagation induced by such a flow event is very short-lived and localized [91]. Therefore, we can put our attention on the cage. Under shear, the cage slightly deforms [112–114] and rearranges quickly after a jump time τ_{sh} . The massive and successive cage jumps in a fast region result in a stress evolution that is relatively stationary, without an overall stress accumulation process. To model the cycle of fast cells, however, we still assume a deformation–yielding process, as illustrated in Fig. 14 (c). This form should not be viewed as the evolution of a solid-like cluster. On the contrary, it represents the averaged *cage distortion–cage jump* process in a fast cell. Notice that, here we still use G_{eff} as the slope of stress, as shown in Fig. 14 (c). In principle, the modulus here should be smaller than that of solid-like regions. However, considering that modulus is not very sensitive to relaxation time [80], we adopt G_{eff} for fast cells as an acceptable approximation. By assuming a similar apparent form of cycle for both fast and slow cells, we simplify the calculation of our model.

After the first cycle, a cell will sample a new τ_{LC} , which corresponds to new τ_{LC}^{th} and τ_{sh}^{th} . Then, the next cycle starts. The treatment is the same: The new cycle will be identified as slow or fast. Then, it evolves following the corresponding form of cycle. This process will be carried out repeatedly. Here, we still use $H_{eq}(\tau_{LC})$ for sampling τ_{LC} of subsequent cycles. The stress of the system is given by the average stress of all cells. In this model, for a specific sample, the only free adjustable parameter is the restructuring strain γ_{res} .

In Fig. 15, we compare the start-up stress predicted by our model with the accurate results for both samples. In each column, we display the stress evolutions of slow particles, fast particles, and the whole system in sequence for a specific sample. Here, “slow” and “fast” denote the classification at the beginning of shear. It is seen that this simple model captures some essential features:

(i) For slow particles, stress exhibits a pronounced overshoot before yielding. Both the magnitude of the stress overshoot and the yielding strain increase with $\dot{\gamma}$.

(ii) For fast particles, the stress evolves in a smoother way, which can be described by $\sigma(t) \propto [1 - \exp(-t/\tau_f)]$. The waiting time prior to steady state τ_f decreases as $\dot{\gamma}$ increases.

There are some aspects that our model does not well align with the MD results, particularly at large shear rates. First, our model displays an undershoot following the overshoot. This undershoot arises from our assumption that τ_{sh}^{th} is solely determined from τ_{LC}^{th} through Eq. 4. In reality, there could be other uncertainties in this relation. By incorporating additional parameter, such as the yielding rate [105], this undershoot can be mitigated. More notably, the model overestimates the yielding strain for shear rates within the shear-thinning regime. This problem should be related to the fact that at high shear rates, the majority of the system behaves as solid-like regions. In this case, the behaviors of different cells are inevitably correlated by the elasticity-mediated interaction. As discussed above, the key difference between our model and EPM is that our model does not incorporate the correlation between different cells, while EPM does. Following this line of thought, we perform an EPM analysis [92, 105, 111, 115] on our samples. The details of the EPM we use will be given in a separated paper. In Fig. 15 (e), we plot the EPM predictions for sample A at $\dot{\gamma} = 0.00025$ and 0.0011 . It is seen that for $\dot{\gamma} = 0.0011$ (within the shear-thinning regime), the EPM gives a better prediction on the yielding strain than our model. However, at $\dot{\gamma} = 0.00025$ (within the crossover regime), for which the solid-like behavior is not dominant, the performance of EPM is worse than our model. The reason could be that the inter-cell correlation mediated by elasticity, which is essential in EPM, is weak here due to the presence of massive liquid-like regions. In principle, EPM treats the mechanical behavior from the viewpoint of solids. On the contrary, the starting point of our model is the viewpoint of supercooled liquids—the heterogeneities in dynamics and response. Considering these results, a possible improvement of our model is to introduce the inter-cell correlation between adjacent solid-like cells. This work is in progress.

IV. STRUCTURAL BASIS

The above analysis shows that the intricate flow behaviors of supercooled liquids can be understood by focusing on τ_{sh} and τ_{LC} , which are connected by the relation

$\tau_{sh}(\tau_{LC})$ given by Eq. 4. There are several key observations related to τ_{sh} and τ_{LC} : First, τ_{LC} exhibits DH features, in the sense that τ_{LC} exhibits a broad distribution and significant clustering in space. Second, the functional form of $\tau_{sh}(\tau_{LC})$ of a liquid is universal once the final shear rate is given. To be specific, it converts a τ_{LC} value to the corresponding τ_{sh} , regardless of the configuration from which τ_{LC} is extracted. The degeneracy of τ_{LC} implies that there exists an underlying configurational parameter (or a set of parameters) that can be applied to both equilibrium and shear states to determine the τ_{LC} value through the same functional form. Third, as the final shear rate increases, $\tau_{sh}(\tau_{LC})$ bends at smaller τ_{LC} with more remarkable flattening. This change directly leads to the increase of the solid-like component in flow, which critically enhances shear thinning. Here, a question arises: How can we understand these dynamical behaviors within a unified framework?

As we mentioned in Sec. I, in the last two decades, substantial efforts have been made to explore the role of structure in determining dynamics of supercooled liquids and glasses. Inspired by this thinking, in this section, we aim to seek the structural basis of the dynamical behaviors mentioned in the preceding paragraph. The key is to construct a parameter or a set of parameters using the structural properties of equilibrium state and shear states with various $\dot{\gamma}$. By employing this structural parameter, we reveal a connection between microscopic structure and dynamics for flowing supercooled liquids. This connection, together with the established relation between τ_{LC} and rheology, creates a pathway from microscopic structure to macroscopic flow behavior.

The discussion in this section is based on the condition of steady shear. The conclusions can also be applied to the start-up shear.

A. Structural parameters for τ_{LC}

We first establish the connection between τ_{LC} and configuration. In literature of supercooled liquids and glasses, numerous structural parameters have been proposed to predict dynamics, ranging from simple, physically informed metrics to more complex ones. Some examples include free volume [36, 116], local favored structures [37, 45], soft modes [25], structural entropy [35], etc. In recent years, approaches based on statistical learning have gained prominence [28, 32–34]. Especially, some sophisticated models, such as graph neural network [33, 117] and multilayer perceptron [118], have been employed and achieved unprecedentedly high prediction accuracies compared with the single, simpler parameters, albeit at the cost of being order-agnostic. Notably, linear regression method offers a balance between high prediction accuracy and interpretability. Another advantage of linear regress method is that it does not need a very large data set. In previous studies [34, 119], Filion et al. have connected the local structure of reference particle

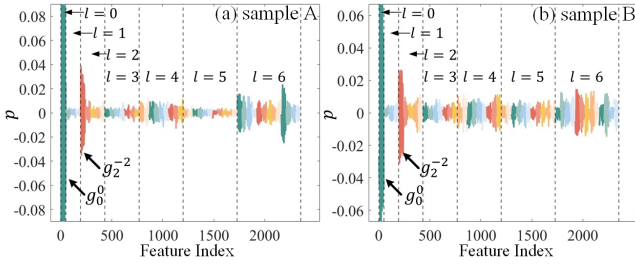


FIG. 16. Correlation between τ_{LC} and the local structural feature defined by Eq. 9. (a) and (b) give the results of sample A and sample B, respectively. The correlation is characterized by the Pearson correlation coefficient p . The horizontal axis represents the element in the feature vector. Each element is characterized by l , m and r (only big particles are considered here). l ranges from 0 to 6, dividing the horizontal coordinates into 7 regimes separated by vertical dashed lines. For each l , the values of m are arranged from $-l$ to l . Different m features with the same l are distinguished by different colors. For each (l, m) combination, there are 48 values of r . In total, there are 2352 elements are shown. Two prominent peaks are highlighted by black arrows, representing the features constructed using g_0^0 and g_2^{-2} .

to its dynamic propensity using linear regression, which achieves an accuracy comparable to that of more complex models. In this subsection, linear regression will be used to connect τ_{LC} and local configuration.

The first step is to construct a data set to train the model. Here, we include configurations under steady shear with all studied shear rates in our data set. Specifically, the shear rates span from the Newtonian regime to the shear-thinning regime. For each $\dot{\gamma}$, we extract 10 configurations in the steady state. The time interval between adjacent configurations is greater than $4\tau_\alpha$, where τ_α is the α relaxation time at the corresponding state. We then measure τ_{LC} for every particle in each configuration in the data set. Additionally, we have verified that including more configurations does not alter our main findings.

Next, for a reference particle i in a given configuration, we use the following quantity to describe its local configuration, as suggested by Ref. [34]:

$$g_{l,i}^m(s, r) = \frac{1}{r^2} \sum_{j \in s} \exp \left[-\frac{(r - r_{ij})^2}{2\delta^2} \right] Y_l^m(\mathbf{r}_{ij}), \quad (9)$$

where r denotes the distance to particle i , r_{ij} is the displacement between particle j and particle i , s denotes the species of particles (big or small) whose distribution we want to probe, and $Y_l^m(\mathbf{r}_{ij})$ is the (l, m) -order spherical harmonic function. It can be seen that $g_{l,i}^m(s, r)$ gives the spherical harmonic expansion coefficient of the transient density of neighbors belonging to species s at distance r from the reference particle i . To ensure that the density varies smoothly in space, we use a Gaussian density with a width δ in the sum. We set $\delta = 0.1$, and consider 48 values of r including 0.3, 0.4, 0.5, \dots , 5.0.

For a given combination of (l, m) , the feature vector g_l^m comprises 96 elements, involving 48 r values and 2 species. In principle, one may include numerous (l, m) combinations to formulate the total feature vector for a particle. However, too many (l, m) combinations would yield a feature vector that is cumbersome and computationally intensive. To make our feature representation as simple as possible, it is necessary to judiciously select a subset of (l, m) combinations to serve as the major features. For this purpose, we examine the importance of every (l, m) combination in affecting dynamics up to $l = 6$ by computing the Pearson correlation coefficient p between each element in the feature vector with respect to the given (l, m) and the target property τ_{LC} . For the sake of simplicity, only big particles are considered here. Thus, 48 elements, covering all r values, are examined for a (l, m) combination. Considering that the number of (l, m) combinations up to $l = 6$ is 49, we examine $48 \times 49 = 2352$ elements in total for each sample. Figure 16 shows the results. The horizontal axis represents the feature index ranging from 1 to 2352. These indexes are divided into 7 regimes according to the value of l . For each l , the values of m are arranged from $-l$ to l ; and for each (l, m) combination, the values of r are arranged from 0.3 to 5.0 in Fig. 16. Two prominent peaks in Fig. 16 are seen, respectively corresponding to $(l = 0, m = 0)$ and $(l = 2, m = -2)$. The $(l = 0, m = 0)$ features reflect the packing efficiency around the reference particle, and it has been reported that local packing capacity is highly correlated with dynamics [26, 29]. The $(l = 2, m = -2)$ features have a symmetry consistent with the shear geometry [42, 113, 114], and thus reflect the local shear strain [42, 72, 78, 120]. As discussed in the previous sections, different τ_{LC} values correspond to different deformation phases in solid-like regions. A larger local strain indicates that it is closer to the local yielding point, leading to greater instability. Thus, the high correlation of $(l = 2, m = -2)$ features is expected. In passing, the importance of the local packing and configurational distortion in the dynamics and rheology of supercooled liquids has been highlighted in recent studies [121, 122]. It is also seen that features corresponding to $l = 6$ show relatively high correlation. This is consistent with the studies reporting the existence of icosahedral pattern in supercooled liquids, which is strongly correlated with dynamics [123, 124].

According to the observation shown in Fig. 16, we use the features with $(l = 0, m = 0)$ and $(l = 2, m = -2)$ to construct the feature vector. For particle i , the feature vector is given by:

$$X_i^{(0)} = (g_{0,i}^0(s, r), g_{2,i}^{-2}(s, r)). \quad (10)$$

Incorporating both species and 48 r values, the elements of $X_i^{(0)}$ amount to 192. The superscript “(0)” denotes that this is the zeroth generation of a series of feature vectors.

It is seen that both solid-like and liquid-like regions are spatially extended, indicating the existence of medium-

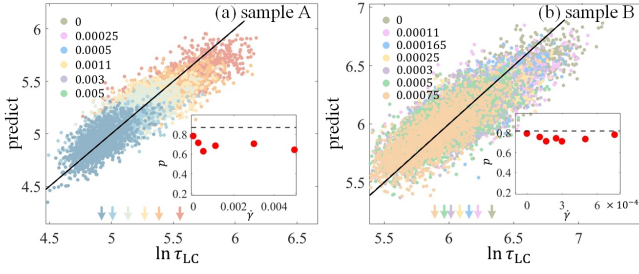


FIG. 17. Comparison between the true values of $\ln(\tau_{cr})$ and the values predicted by the linear regression model for particles extracted from configurations at various $\dot{\gamma}$. (a) and (b) show the results of sample A and sample B, respectively. Each point corresponds to a particle. Points belonging to the same $\dot{\gamma}$ are in the same color. Black solid lines denote the situation that the predicted value equals to the true value. Arrows positioned at the bottom of panels indicate the average $\ln(\tau_{cr})$ for each $\dot{\gamma}$. Inset: Pearson correlation coefficient between the true and predicted values of $\ln(\tau_{cr})$ for each $\dot{\gamma}$. Horizontal dashed line represents the Pearson correlation coefficient calculated using the data across all $\dot{\gamma}$.

ranged order. In literature, medium-ranged orders have also been emphasized on glass transition [124–127]. To incorporate this medium-ranged structural effect, we adopt a coarse-graining method [29, 34]. Specifically, the next generation of the feature vector is produced by coarse-graining the last generation by:

$$X_i^{(n+1)} = \frac{1}{Z} \sum_{j, r_{ij} < r_c} \exp\left(-\frac{r_{ij}}{r_c}\right) X_j^{(n)}, \quad (11)$$

where r_c is a parameter characterizing the range of coarse-graining and is set to 4, and Z is written as:

$$Z = \sum_{j, r_{ij} < r_c} \exp\left(-\frac{r_{ij}}{r_c}\right). \quad (12)$$

Another advantage of the coarse-graining is that it averages out irrelevant thermal noise. With Eqs. 10 and 11, we construct the final feature vector for particle i by combining the feature vectors with generations 0, 1 and 2:

$$X_i = (X_i^{(0)}, X_i^{(1)}, X_i^{(2)}). \quad (13)$$

There are 576 elements in X_i .

Now, we try to establish the connection between τ_{LC} and the local configuration represented by X_i . Note that, in many studies on glass transition, researchers explore the connection between τ_α and structural parameters through a Vogel-Fulcher-Tammann form [128, 129]. Inspired by this approach, we transform τ_{LC} to $\ln \tau_{LC}$ and employ the Ridge linear regression model [130] to establish the correlation between feature vectors and $\ln \tau_{LC}$. Such a transformation will be further rationalized in the next section.

We randomly split our data set with a ratio of 8 : 2, with 80% of the data used for training and the remaining 20% used for testing. Figure 17 compares the true

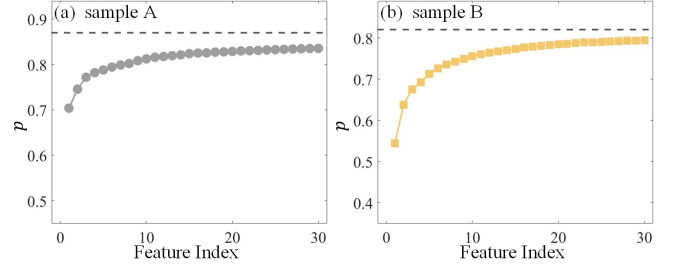


FIG. 18. Cumulative Pearson correlation coefficients of the top 30 most important elements in the feature vector defined by Eq. 13. (a) and (b) show the results of sample A and sample B, respectively. The dashed line in each panel denotes the Pearson correlation coefficient obtained with the entire feature vector.

values of $\ln \tau_{LC}$ and the values predicted by the regression model for the test set, where each point represents a particle. Here, results under steady shear with various $\dot{\gamma}$, including equilibrium, Newtonian, crossover, and shear-thinning regimes, are plotted together. These results suggest a positive correlation between the predicted and true values of $\ln \tau_{LC}$, quantified by the Pearson correlation coefficient p of 0.87 for sample A, and 0.82 for sample B. We also calculate the Pearson correlation coefficient for each $\dot{\gamma}$. The results, given in the insets of Fig. 17, are around 0.7. It is seen that the correlation for single $\dot{\gamma}$ remains robust. The good correlations shown in Fig. 17 suggest that the structural parameters used here are applicable to both equilibrium and a wide range of $\dot{\gamma}$.

An important observation from Fig. 17 is that the data points corresponding to different $\dot{\gamma}$ approximately align along the same truth line. This consistency suggests the existence of a common structural basis for τ_{LC} that is invariant to the applied shear. As a result, we unify the τ_{LC} found from equilibrium and shear states by leveraging these structural parameters.

One may argue that the 576 elements contained in one feature vector given by Eq. 13 are still too many, which calls for further interpretation and simplification. We sort these elements according to their contributions to the cumulative Pearson correlation coefficient. Figure 18 gives the cumulative Pearson correlation coefficients of the top 30 most important elements in sorting sequence. It is seen that the first several elements contribute the majority of the total correlation, while the remaining ones' contribution is marginal. The detailed sequences of important elements for both samples are given in Appendix C.

B. Structural basis for solid-liquid duality

In the preceding subsection, τ_{LC} extracted from different $\dot{\gamma}$ have been quantified through a unified viewpoint of structure. Moreover, in Sec. II, we reveal a firm relation between the local response and the local dynamics.

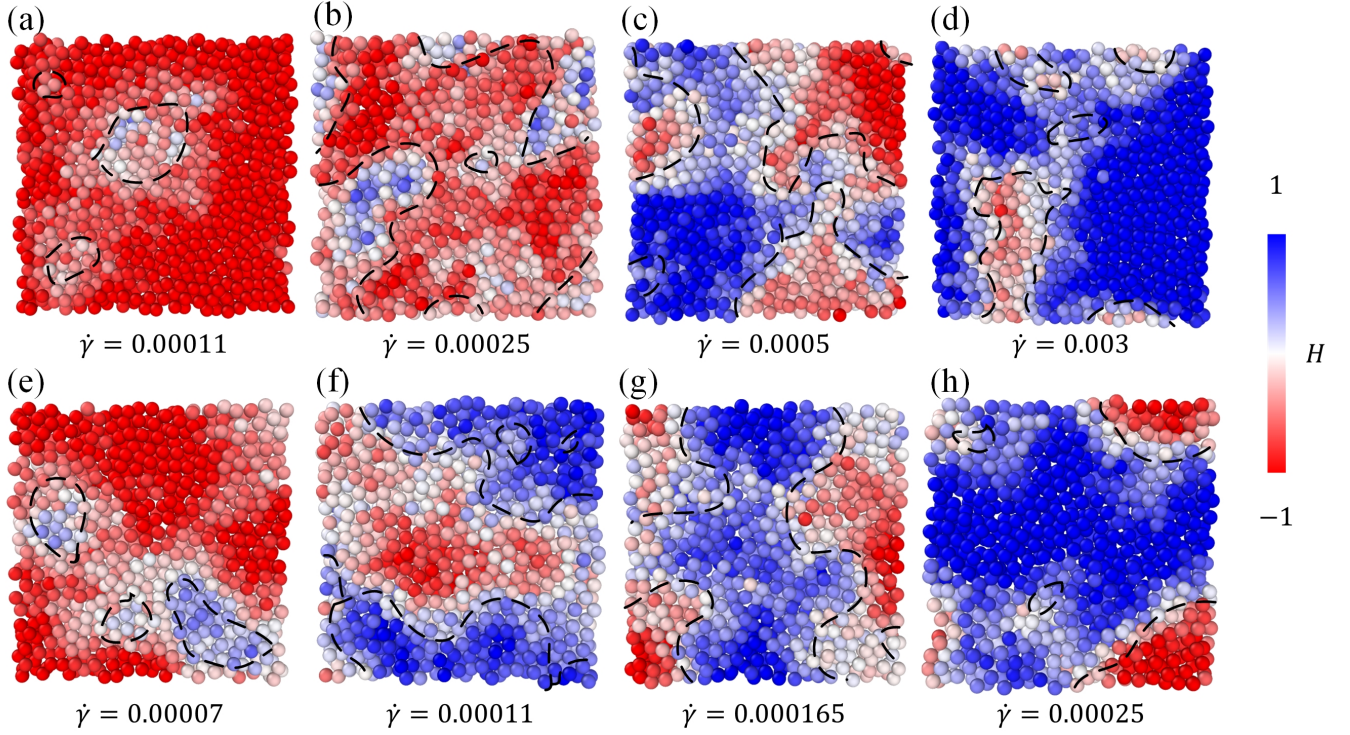


FIG. 19. Spatial distributions of the hardness H at various $\dot{\gamma}$ for both samples. (a) – (d) show the configuration slices selected at different $\dot{\gamma}$ for sample A. (e) – (h) show the configuration slices selected at different $\dot{\gamma}$ for sample B. In all panels, the color of each particle denotes its value of H with a common color bar. The boundaries between liquid-like (fast) and solid-like (slow) groups are denoted by black dashed lines. A nice agreement between the boundaries and the particles with H close to 0 is seen in all panels.

Therefore, one may expect a structural basis for the local response. Particularly, we have demonstrated that the local response has two forms: solid-like and liquid-like. As $\dot{\gamma}$ increases, the ratio of these two components varies, corresponding to the flattening of the form of $\tau_{\text{sh}}(\tau_{\text{LC}})$. Here, we aim to comprehend such variation with the assistance of structural parameters. The key is to find a structural criterion, which is universal for all shear rates, for classifying particles into solid-like and liquid-like groups.

In the study of amorphous solids, research focusing on identifying soft spots that are more susceptible and likely to transform into STZs based on structural information is highly active. Ref. [32] gives a comprehensive review on this topic. Recently, such research was advanced by a pioneering study [28], in which the soft spots in amorphous solids are identified by employing support vector machine (SVM) [130]. To be specific, the authors firstly define a structural feature vector for particles. By viewing each particle as a point in the high-dimensional space defined by the feature vector, the SVM can identify a hyperplane in this space that optimally separates particles into two categories according to their nonaffine displacements under deformation. Particles located at the side of the hyperplane featured by large nonaffine displacements are considered as soft spots. Furthermore, the authors define the *softness* parameter for each particle by its dis-

tance to the hyperplane. Particles with higher softness are more likely to undergo rearrangement under shear.

Inspired by Ref. [28], we use SVM to explore the structural basis of the solid-liquid duality of the local response. It is worth noting that there is a fundamental difference between the considerations of Ref. [28] and our work. In the study of the deformation of amorphous solids such as Ref. [28], the key question is to figure out *why and how a solid flows*. A soft spot is a liquid-like region in the solid background, which plays as the precursor of the bulk yielding and flow. For supercooled liquids, on the contrary, the key question is shifted to *why a liquid exhibits strong viscoelasticity* [42]. Consequently, the focus of our work is shifted to the hard regions, i.e., the solid-like regions in the liquid background [42, 78–80].

Here, we still use the feature vector introduced in Eq. 13 to characterize the local structure of each particle. To construct the data set for the SVM model, we select 10 configurations from each $\dot{\gamma}$, ranging from the equilibrium state to the shear-thinning regime. For each configuration, particles are classified as slow and fast using the method given in Sec. II. Slow particles are assigned to the solid-like group G_s , while fast particles are assigned to the liquid-like group G_l . The number of elements in G_s and that in G_l are set to be equal. The data set is randomly partitioned into a training set and a test set

with a ratio of 8 : 2. Particles in G_s are labeled as 5, while those in G_l are labeled as -5. Then, a SVM algorithm with a linear kernel is employed on the training set. The penalty factor is finely tuned to achieve the optimal classification. With this operation, we construct a hyperplane in the high dimensional space defined by the feature vector to separate the two categories of particles. We examine the accuracy of the classification with the test set, and the result is 82%.

Moreover, we calculate the distance to the hyperplane for each particle. Positive and negative values of the distance represent solid-like and liquid-like particles, respectively. This distance is expected to reflect the extent to which the particle exhibits solid-like response. Thus, we term it as the *hardness* of particle, denoted as H . Considering that the classification of response is related to τ_{LC} , we expect that H and τ_{LC} is positively correlated. We test their correlation with the test set. The Pearson correlation coefficients of H and τ_{LC} are about 0.5 for all shear rates and both samples.

To validate our SVM model, it is crucial to check if it can correctly capture the solid-like and liquid-like regions. In Fig. 19, we plot several slices of both systems at different $\dot{\gamma}$. The upper and lower panels represent sample A and sample B, respectively. Particles are colored based on their values of H . We also plot the boundary between fast and slow regions for all slices according to the method given in Sec. II with black dashed lines. It is seen that the two methods give highly consistent spatial features of the solid-liquid duality in local response.

There is another important observation from Fig. 19. Firstly, we recall that the model for determining H is universal and valid for all shear rates. Then, as shown in Fig. 19, we find that more particles migrate to the $H > 0$ side with the growth of $\dot{\gamma}$. To quantify this observation, we calculate the average value of H over all particles \bar{H} for each $\dot{\gamma}$ and both samples. The results are given in Fig. 20 (a) and (b). As $\dot{\gamma}$ increases, \bar{H} starts to increase from a negative value, passes through zero, and finally becomes positive. It is interesting to see that the shear rate at which \bar{H} crosses zero just coincides with the crossover regime. We can evaluate the percentage of slow particles by calculating the proportion of particles with $H > 0$. The results, denoted as p_H , are shown in Fig. 20 (c) and (d) for sample A and sample B, respectively. Meanwhile, we replot the results of p_{slow} shown in Fig. 13. It is seen that p_H and p_{slow} are consistent with each other. This agreement provides a structural view for the shear-induced changes in dynamics and local response.

The result discussed in this subsection makes an advance to the preceding subsection. In the preceding subsection, we find the correlation between structure and τ_{LC} . This correlation is somewhat natural: By definition, τ_{LC} is calculated by using the ICE method and stopping external shear. In this way, the convection and thermal noise are removed, which highlights the role of the transient configuration in determining τ_{LC} . This correlation

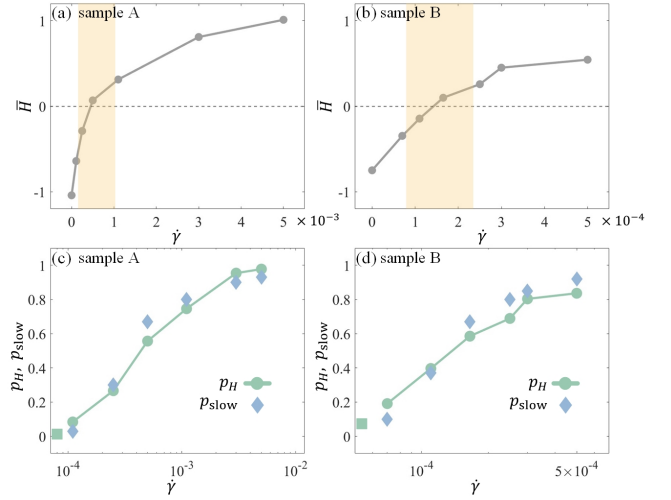


FIG. 20. (a) and (b) show the variation of the configuration-averaged H , denoted as \bar{H} , with respect to $\dot{\gamma}$ for sample A and sample B, respectively. In both (a) and (b), vertical yellow bands denote the crossover regime. (c) and (d) show the proportion p_H of particles with $H > 0$ (circles and squares) for sample A and sample B, respectively. Squares denote the results at the equilibrium state, and circles denote the results at other shear rates. In both (c) and (d), the results of p_{slow} (diamonds), which have been shown in Fig. 13, are replotted.

is irrelevant to local response to shear and the form of $\tau_{sh}(\tau_{LC})$. In this subsection, by utilizing the same feature vector, we build the connection between local response and local structure. Note that the form of local response involves the interplay among external shear, thermal activation and structure. The effectiveness of H in classification and the variations of \bar{H} and p_H with $\dot{\gamma}$ further emphasize the importance of local structure in determining the rheology of supercooled liquids. Summarizing all results in this section, we establish the structural basis for the dynamical and rheological behaviors discussed in Secs. II and III.

V. DISCUSSION: A PEL PERSPECTIVE

In Secs. II – IV, we find the connection from the local configuration to the local dynamics and response, and finally to the flow behaviors. Following this line of thought, one may expect to formulate the behaviors of τ_{LC} , the form of $\tau_{sh}(\tau_{LC})$, and the duality in local response, which compose the foundation for understanding the flow of supercooled liquids in our framework, with theoretical tools involving local configuration and dynamics. The key issue is to elucidate how the structure, flow and thermal effect collectively affect the local dynamics. In this section, this problem will be discussed by utilizing and modestly extending several critical ingredients of the PEL picture.

A. PEL perspective on τ_{LC} and τ_{sh}

Supercooled liquids are featured by amorphous configuration and slow dynamics [15, 56, 80]. PEL provides a useful way to bridge these two features [47–49]. In this picture, the potential energy of the system, which is a function of coordinates of all particles, defines a complex $3N$ -dimensional surface composed of numerous basins. For a supercooled liquid, the system is trapped in basins for most of the time, and undergoes inter-basin jumps occasionally by thermal activation [47, 49, 58].

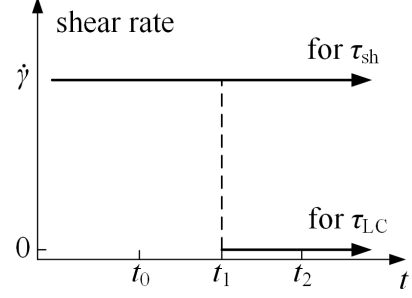
Despite the convenience and clearness in concept, the effectiveness and complexity of PEL method get worse for big systems [47], because the inter-basin jump of big systems is very frequent and its effect is not so sharp. On the other hand, trap model provides an effective approach for understanding the slow dynamics [109, 131]. In this model, the whole system is divided into many coherent subsystems. For each subsystem, the picture of PEL is applied: the subsystem is confined in basins (traps) separated by barriers that can be overcome by thermal activation. The dynamics of the whole system is related to the statistics of the configuration of subsystem.

PEL is tilted as shear is applied. As strain increases, the degree of tilt and elastic stress are both enhanced, until mechanical instability emerges [50, 132]. Then, the shear stress is released, and the system goes into next minimum. For glasses under steady shear, such stress buildup and strain-activated process take place successively, which plays a key role in the non-Newtonian behavior [133].

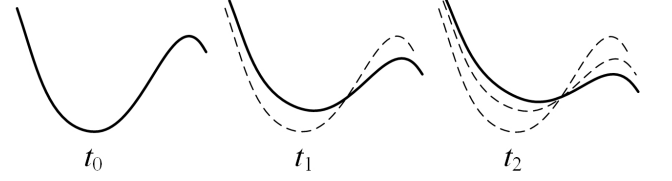
In this subsection, we will model the behaviors of τ_{LC} and τ_{sh} by combining the ideas discussed in the above three paragraphs. Considering that both τ_{LC} and τ_{sh} are defined as the time for a reference particle to jump out, we can assume a basin for the particle to represent the potential energy barrier it experiences [26]. The shape of the basin is determined by the local configuration of the reference particle. When shear is applied, the basin is tilted. In Fig. 21 (a), we review the flow conditions for extracting τ_{LC} and τ_{sh} with respect to the configuration at $t = t_1$. Figure 21 (b) illustrates the evolution of PEL for measuring τ_{sh} . In this case, the shear is steady, and the PEL tilts more and more with time before the mechanical instability. Figure 21 (c) illustrates the evolution of PEL for measuring τ_{LC} . Here, the external shear stops at $t = t_1$. Consequently, the basin also stops tilting at $t = t_1$. Figure 21 elucidates the difference between τ_{LC} and τ_{sh} . τ_{sh} describes the local relaxation in flow. It is determined by the combined effect of thermal activation and convection. For τ_{LC} , the convection is eliminated by stopping external shear and, thus, it is determined by the thermal activation from the distorted configuration at $t = t_1$. From the above discussion, it is seen that τ_{LC} , rather than τ_{sh} , directly reflects the local configuration and the particle-level energy barrier.

Now we put our attention on the particle-level basin. We denote the energy barrier of the basin at zero strain as

(a) flow condition



(b) for τ_{sh}



(c) for τ_{LC}

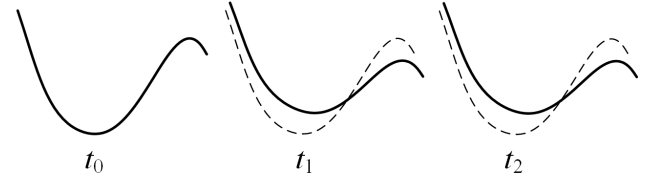


FIG. 21. (a) A review of the flow conditions for measuring τ_{LC} and τ_{sh} under steady shear with respect to a configuration at time t_1 . (b) Illustration of the evolution of PEL for measuring τ_{sh} under steady shear. Here, the PEL shows an increasing tilt as time goes, represented by the change in shape from dashed lines to solid lines. (c) Illustration of the evolution of PEL for measuring τ_{LC} . Here, the tilting of PEL stops at $t = t_1$ due to the abrupt cession of flow.

E_b . Without external shear, the probability of thermal activation occurring within a small time interval dt is proportional to $\Gamma \exp(-E_b/k_B T) dt$, where Γ is the attempt frequency. The value of E_b varies in space [134, 135]. According to the activation picture, E_b is related to τ_{LC} at equilibrium by:

$$\tau_{LC,eq} \sim \frac{1}{\Gamma} \exp\left(\frac{E_b}{k_B T}\right), \quad (14)$$

where $\tau_{LC,eq}$ denotes the τ_{LC} at equilibrium. With Eq. 14 and the spectrum of $\tau_{LC,eq}$, the distribution of E_b can be obtained.

In the presence of external shear, the local structure undergoes deformation at a strain rate of $\dot{\gamma}$. During the deformation, the local structure will store potential energy until the activation takes place. This deformation energy is denoted as $E(\gamma)$, where γ is the local strain. Taking into account both thermal activation and shear-induced deformation, the probability for a particle to es-

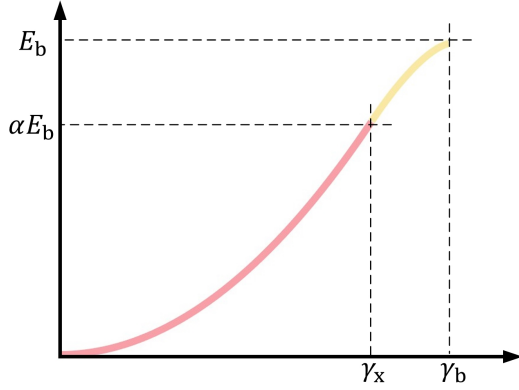


FIG. 22. Illustration of the deformation energy $E(\gamma)$ given by Eq. 16. The harmonic part is colored by light red, and the catastrophe part is colored by yellow. γ_x denotes the boundary between these two parts. αE_b ($0 < \alpha < 1$) gives the value of $E(\gamma = \gamma_x)$.

cape the basin within dt is given by:

$$\Gamma \exp \left[-\frac{E_b - E(\dot{\gamma}t)}{k_B T} \right] dt. \quad (15)$$

Here, the form of $E(\gamma)$ is important. For small strain, $E(\gamma)$ is harmonic. However, as γ increases, $E(\gamma)$ gradually deviates from the harmonic form. As predicted by the catastrophe theory, when γ approaches the edge of basin γ_b , the energy increment ΔE scales with the residual load $\gamma_b - \gamma$ as $\Delta E \propto (\gamma_b - \gamma)^{3/2}$ [136]. Moreover, Maloney and Lacks demonstrate that this scaling remains valid well beyond the vanishing regime of $\gamma_b - \gamma$, even at finite temperatures [137]. Considering the behaviors of $E(\gamma)$ at small and large strains, we model its form as:

$$E(\gamma) = \begin{cases} \frac{1}{2} G \Omega \gamma^2 & 0 \leq \gamma \leq \gamma_x \\ E_b - A(\gamma_b - \gamma)^{3/2} & \gamma_x < \gamma \leq \gamma_b \end{cases}, \quad (16)$$

where G is the local shear modulus, Ω is the activation volume, γ_x is the crossover strain, and A is a numerical factor. Figure 22 illustrates the form of $E(\gamma)$. By requiring that both $E(\gamma)$ and its first-order derivative are continuous at $\gamma = \gamma_x$, the three parameters, γ_x , γ_b and A , can be reduced to a single parameter. As illustrated in Fig. 22, we can denote the value of $E(\gamma_x)$ by αE_b , where α ($\alpha \in (0, 1)$) is employed as the free adjustable parameter that represents γ_x , γ_b and A .

Besides the free parameter α , other parameters in Eq. 15 are set as follows: Γ^{-1} is determined from the MSD data at equilibrium as the time at which the particle enters the plateau regime. G is set to the effective modulus G_{eff} defined in Sec. III. Ω represents the size that will be involved for the reference particle to jump out. At the current stage, we estimate Ω by the volume of the cage, i.e., the sphere whose radius is given by the distance of the first minimum of $g(r)$. For the sake of simplicity, we assume that all these parameters do not

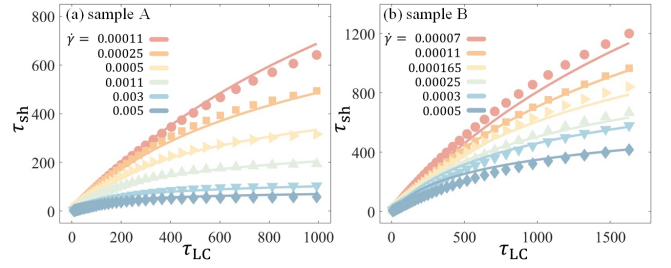


FIG. 23. $\tau_{\text{sh}}(\tau_{\text{LC}})$ calculated from the PEL model (lines) for sample A (a) and sample B (b) at various $\dot{\gamma}$. The results obtained from MD data (symbols) are also plotted. In each panel, the results corresponding to the same $\dot{\gamma}$ are displayed in the same color.

vary with $\dot{\gamma}$. Note that our assumption on Ω is oversimplified. As demonstrated in Sec. III, the component of solid-like parts increases with $\dot{\gamma}$, which may result in the enhancement of the correlation between particles. We will revisit this point in Sec. V C.

Assuming that the basin starts deforming at $t = 0$, the probability that a particle jumps at t can be derived with Eq. 15 and is expressed as:

$$f(t) = \Gamma \exp \left[-\frac{E_b - E(\dot{\gamma}t)}{k_B T} \right] \times \exp \left(-\Gamma \int_0^t \exp \left[-\frac{E_b - E(\dot{\gamma}t')}{k_B T} \right] dt' \right). \quad (17)$$

Then, we can calculate the mean waiting time of jump by:

$$\begin{aligned} \bar{t}(E_b, \dot{\gamma}) &= \int_0^\infty t f(t) dt \\ &= \int_0^\infty \exp \left(-\Gamma \int_0^t \exp \left[-\frac{E_b - E(\dot{\gamma}t')}{k_B T} \right] dt' \right) dt. \end{aligned} \quad (18)$$

Setting $\dot{\gamma} = 0$, Eq. 18 reduces to Eq. 14 and gives the value of τ_{LC} at equilibrium. For $\dot{\gamma} > 0$, $\bar{t}(E_b, \dot{\gamma})$ gives τ_{sh} according to the picture shown in Fig. 21. Therefore, with Eq. 18, we can get the form of $\tau_{\text{sh}}(\tau_{\text{LC}})$. Figure 23 shows $\tau_{\text{sh}}(\tau_{\text{LC}})$ found by the PEL model at various $\dot{\gamma}$ for both samples. For comparison, we also plot the MD results of $\tau_{\text{sh}}(\tau_{\text{LC}})$. It is seen that the PEL model captures the general characteristics of $\tau_{\text{sh}}(\tau_{\text{LC}})$. Particularly, its form exhibits a greater flattening with $\dot{\gamma}$. From the viewpoint of this model, this flattening is due to the increasingly dominant role of shear deformation compared to thermal activation as $\dot{\gamma}$ increases.

Figure 24 (a) shows $f(t)$ at different $\dot{\gamma}$. To calculate $f(t)$, we set E_b in Eq. 17 with the most probable value of the equilibrium distribution of E_b of sample A, denoted as E'_b . As $\dot{\gamma}$ increases, $f(t)$ as a whole shifts to smaller t . Moreover, the form of $f(t)$ also changes with $\dot{\gamma}$. In Fig. 24 (b), we plot the scaled $f(t)$, denoted as $f^*(t^*)$, where $t^* = t/\bar{t}(E'_b, \dot{\gamma})$ and $f^* = f/f_{\text{max}}$ (f_{max} is the maximum value of $f(t)$). It is seen that $f(t)$ gradually

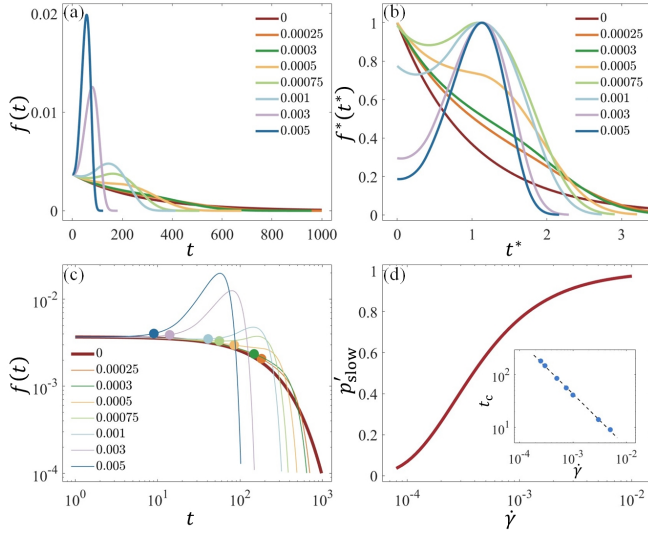


FIG. 24. Functional forms of $f(t)$ as various $\dot{\gamma}$. (a) $f(t)$ in linear scale. (b) $f^*(t^*)$, where $t^* = t/\bar{l}(E_b, \dot{\gamma})$ and $f^* = f/f_{\max}$. (c) $f(t)$ in log-log scale. The form at equilibrium $f_{\text{eq}}(t)$ is highlighted by a thick line. For each $\dot{\gamma}$, we mark the position t_c at which $f(t)$ deviates from $f_{\text{eq}}(t)$ by a circle with its color the same to that of the corresponding $\dot{\gamma}$. (d) The proportion of slow particles found from the PEL analysis p'_{slow} as a function of $\dot{\gamma}$. Inset: t_c as a function of $\dot{\gamma}$ in log-log scale (symbols). The dashed line denotes the relation $t_c \sim \dot{\gamma}^{-1}$.

changes from an exponential form to a gaussian-like form as $\dot{\gamma}$ increases. Particularly, for intermediate shear rates, $f(t)$ exhibits a bimodal form composed of an exponential component and a gaussian component, with the gaussian component being enhanced by $\dot{\gamma}$.

The alternation of the form of $f(t)$ corresponds to the observation in Secs. II and III that more particles are accelerated by shear as $\dot{\gamma}$ increases. To clarify this point, we plot $f(t)$ in the log-log scale in Fig. 24 (c). The one at equilibrium, $f_{\text{eq}}(t)$, is highlighted by a thick solid line. For $f(t)$ with finite $\dot{\gamma}$, all of them align with $f_{\text{eq}}(t)$ at small t , and deviate from $f_{\text{eq}}(t)$ at large t . We denote the point at which $f(t)$ deviates from $f_{\text{eq}}(t)$ as t_c , and mark them in Fig. 24 (c). Evidently, t_c can be viewed as the boundary between fast and slow groups: For $t < t_c$, particles are not accelerated by external shear and should be classified as fast; while for $t > t_c$, particles are accelerated and should be classified as slow. Then, we calculate the percentage of slow particles by $p'_{\text{slow}} = \int_{t_c}^{\infty} f(t) dt$, and show the result in Fig. 24 (d). The S-shaped dependence of p'_{slow} on $\lg \dot{\gamma}$ is similar to the results of p_{slow} shown in Fig. 13, which are directly found from the MD results. The inset of Fig. 24 (d) shows t_c as a function of $\dot{\gamma}$ in the log-log scale, which reveals a clear relation of $t_c \propto \dot{\gamma}^{-1}$. This behavior is also consistent with the MD results shown in Fig. 3 (c) and (d).

B. Steady shear

In the preceding subsection, we model τ_{LC} , τ_{sh} and their relation as the interplay among local configuration, convection and thermal activation through the viewpoint of PEL. The discussion is primarily based on the start-up deformation represented by the behavior with respect to a single basin. In this subsection, we will further leverage the PEL picture to rationalize our findings on the steady shear.

By incorporating convective effects, Sollich et al. generalized the trap model to the flow condition, known as the soft glass rheology (SGR) model [23, 138]. For the condition of steady shear, the equation of motion of the SGR model is given by:

$$\frac{\partial P}{\partial t} = -\dot{\gamma} \frac{\partial P}{\partial \gamma} - \Gamma \exp \left[-\frac{E_b - E(\gamma)}{k_B T} \right] P + \Gamma(t) \rho(E_b) \delta(\gamma), \quad (19)$$

where $P = P(E_b, \gamma, t)$ is the probability that a coherent subsystem experiences a local energy barrier of E_b and a local strain of γ at a given time t . In our picture, $P(E_b, \gamma, t)$ describes the dynamics at the particle level. The first term on the right-hand side of Eq. 19 represents the convective effect. The second term represents the activation from the distorted basin, where the energy barrier is given by $E_b - E(\gamma)$. Here, the form of $E(\gamma)$ and the attempt frequency Γ are set to those used in the preceding subsection. The third term represents the process that the yielded subsystems rearrange to new local equilibrium configurations. $\Gamma(t)$ is the total yielding rate, which is given by:

$$\Gamma(t) = \iint \Gamma \exp \left[-\frac{E_b - E(\gamma)}{k_B T} \right] P(E_b, \gamma, t) d\gamma dE_b. \quad (20)$$

$\rho(E_b)$ is the density of states for new barriers. Here, it is assumed that $\rho(E_b)$ does not depend on $\dot{\gamma}$ [23]. Therefore, $\rho(E_b)$ can be obtained from the dynamics of equilibrium state as follows. First, we measure the distribution of τ_{LC} at equilibrium $H_{\text{eq}}(\tau_{\text{LC}})$. Second, assuming the activation picture, we combine $H_{\text{eq}}(\tau_{\text{LC}})$ and Eq. 14 to find the distribution of barrier height $P_b(E_b)$. Then, $\rho(E_b)$ can be found by:

$$\rho(E_b) \sim P_b(E_b) \exp(-E_b/k_B T). \quad (21)$$

The model given by Eqs. 19 – 21 provides a framework for quantifying the flow behaviors under shear.

As demonstrated in Sec. IV, the dynamics and rheology of supercooled liquids are strongly correlated to the local structure. It is interesting to understand this correlation from the PEL perspective. We recall that local structural terms $g_{0,i}^0$ and $g_{2,i}^{-2}$ are most relevant to local dynamics compared to terms with other combinations of l and m . In the PEL picture, local dynamics is determined by the local energy barrier E_b and the local strain γ . As for $g_{0,i}^0$, it represents the local packing surrounding particle i . Notably, a recent work [26] has

established the quantitative connection between the energy barrier for particles and the local packing efficiency characterized by the particle-wise radial particle density, which is similar to $g_{0,i}^0$, for the equilibrium state. Following this result, it is clear that the importance of $g_{0,i}^0$ for local dynamics comes from its remarkable relation to the local energy barrier E_b . Moreover, we find that the terms with $l = 0$ and $m = 0$ alter with $\dot{\gamma}$ only slightly. This result might justify the above approximation that $\rho(E_b)$ is $\dot{\gamma}$ -independent.

Our emphasis will be on local structural terms with $l = 2$ and $m = -2$. This kind of terms has received less attention in previous studies of the equilibrium state. However, they are very important for shear states as shown in Sec. IV. To understand this observation, we first refer to the conclusion that the strain of an affine shear γ_{aff} is proportional to $g_2^{-2}(r)$ [139, 140]:

$$g_2^{-2}(r) \approx -\gamma_{\text{aff}} \left[\frac{1}{\sqrt{15}} r \frac{d}{dr} g_{\text{eq}}(r) \right], \quad (22)$$

where $g_2^{-2}(r)$ is the ($l = 2, m = -2$) coefficient of the spherical harmonic expansion of the global pair distribution function $g(\mathbf{r})$, and $g_{\text{eq}}(r)$ is $g(\mathbf{r})$ at the undeformed state. Equation 22 suggests that $g_{2,i}^{-2}$ directly reflects the strain of the local configuration of particle i . Now, it is crucial to verify that if the strain variable γ in the PEL framework, which can be calculated with the SGR model, can describe the configurational distortion reflected by $g_{2,i}^{-2}$ under steady shear. For this purpose, we perform the following calculations by employing the SGR model given by Eqs. 19 – 21.

According to Eq. 19, it can be demonstrated that the distribution of local strain γ under steady shear is given by the following equation [23, 138]:

$$P_s(\gamma) \sim \int \rho(E_b) \exp \left[-\frac{1}{g(E_b)} \int_0^\gamma e^{E(\gamma')/k_B T} d\gamma' \right] dE_b, \quad (23)$$

where $g(E_b) = \dot{\gamma} e^{E_b/k_B T} / \Gamma$. With the preceding equation, we can find the average local strain $\bar{\gamma}$ under steady shear by:

$$\bar{\gamma} = \frac{\int_0^\infty \gamma P_s(\gamma) d\gamma}{\int_0^\infty P_s(\gamma) d\gamma}. \quad (24)$$

In Sec. IV A, we find that the second generation of $g_{l,i}^m$ well connects the local structure to local dynamics. Here, we adopt the second generation of $g_{2,i}^{-2}$ to represent the local distortion. Moreover, for the sake of simplicity, we do not differentiate particle species when calculating $g_{2,i}^{-2}$ with Eq. 9. With these considerations, we construct the following vector for describing the distortion of the local configuration of particle i :

$$Y_i = (g_{2,i}^{-2}(r_1), g_{2,i}^{-2}(r_2), \dots, g_{2,i}^{-2}(r_n))^{(2)}. \quad (25)$$

Here, the set $\{r_1, r_2, \dots, r_n\}$ gives a series of distances from the reference particle i . With Y_i , we find the average

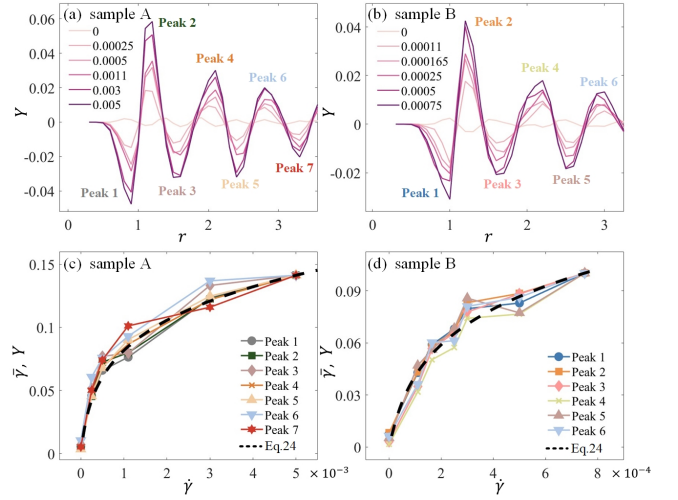


FIG. 25. (a) and (b) show the results of the structure feature Y , defined by Eq. 26, as a function of the distance r at various $\dot{\gamma}$ for sample A and sample B, respectively. The first seven peaks of $Y(r)$ are marked. (c) and (d) show the magnitudes of the first seven peaks of $Y(r)$ (symbols) at different $\dot{\gamma}$ for sample A and sample B, respectively. The results of $\bar{\gamma}$ (dashed lines), defined by Eq. 24, at different $\dot{\gamma}$ are also plotted. In (c) and (d), the values of peak magnitudes of $Y(r)$ are scaled with a numerical factor to compare with $\bar{\gamma}$.

distortion by:

$$Y(r_k) = \frac{1}{N} \sum_{j=1}^N Y_j(r_k), k = 1, 2, \dots, n. \quad (26)$$

We plot the results of $Y(r_k)$ with a series of k values at different $\dot{\gamma}$ for sample A and sample B in Fig. 25 (a) and (b), respectively. $Y(r_k)$ displays an oscillation as r_k increases, which is similar to the r -dependence of $g_2^{-2}(r)$ [42]. As expected, the amplitude of Y grows with $\dot{\gamma}$. Figure 25 (c) and (d) display the magnitudes of the first seven peaks of $Y(r_k)$, which are marked in Fig. 25 (a) and (b), as a function of $\dot{\gamma}$ for sample A and sample B, respectively. Meanwhile, we also plot the results of $\bar{\gamma}$ found from Eq. 24 for both samples in Fig. 25 (c) and (d). It is seen that the magnitudes of the peaks of $Y(r_k)$ and $\bar{\gamma}$ exhibit highly consistent dependences on $\dot{\gamma}$. This consistency holds for different peaks of $Y(r_k)$ within $r_k < 3.5$. At larger r_k , this consistency weakens, implying the localization of such deformation coherency. The remarkable proportionality between $Y(r_k)$ and $\bar{\gamma}$ within $r_k < 3.5$ implies a nice correspondence between $g_{2,i}^{-2}$ and the local strain γ in the PEL framework.

In Sec. IV A, we show that local structural parameters constructed by $g_{0,i}^0$ and $g_{2,i}^{-2}$, which respectively reflect the energy barrier height E_b and the strain γ of the particle-level basin in the PEL framework according to the above discussion, well predict τ_{LC} for all shear rates through a simple linear regression method. To explore the intrinsic mechanism of this correlation between local structure and dynamics, we will evaluate the dependence of τ_{LC} on $\dot{\gamma}$ with the SGR framework. Under steady shear, the

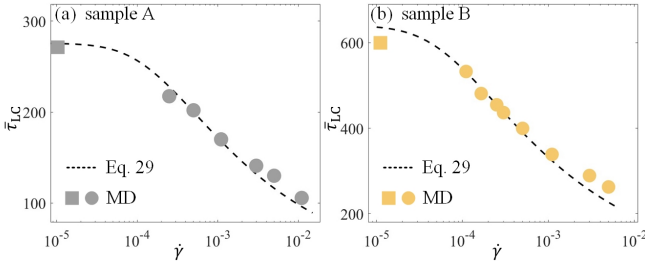


FIG. 26. (a) and (b) show $\bar{\tau}_{LC}$ (dashed lines), defined by Eq. 29, as a function of $\dot{\gamma}$ for sample A and sample B, respectively. Meanwhile, the average τ_{LC} measured from the MD data (symbols) are also shown. For MD results, squares denote the results at the equilibrium state, and circles denote the results for finite shear rates.

distribution of local strain γ and barrier height E_b in the SGR model is given by:

$$P_s(\gamma, E_b) \sim \rho(E_b) \exp \left[-\frac{1}{g(E_b)} \int_0^\gamma e^{E(\gamma')/k_B T} d\gamma' \right]. \quad (27)$$

Within a basin characterized by γ and E_b , the average activation time is given by:

$$\bar{\tau}(E_b, \gamma) = \frac{1}{\Gamma} \exp \left[\frac{E_b - E(\gamma)}{k_B T} \right]. \quad (28)$$

Combining the preceding two equations, the configuration-averaged τ_{LC} , denoted as $\bar{\tau}_{LC}$, is written as

$$\bar{\tau}_{LC} = \frac{\iint P_s(\gamma, E_b) \bar{\tau}(E_b, \gamma) dE_b d\gamma}{\iint P_s(\gamma, E_b) dE_b d\gamma}. \quad (29)$$

Figure 26 gives $\bar{\tau}_{LC}$ as a function of $\dot{\gamma}$ for both samples. We also plot the average $\bar{\tau}_{LC}$ measured directly from MD data in Fig. 26. It is seen that the results found by the SGR model are well consistent with the MD results.

The results shown in Figs. 25 and 26 suggest a clear picture from the PEL perspective for the universal correlation between local structure and τ_{LC} at all shear rates shown in Sec. IV A. The local structural terms related to $g_{0,i}^0$ and $g_{2,i}^{-2}$ respectively associate with the local energy barrier height E_b and the local strain γ of the particle-level basin in the PEL picture. τ_{LC} is the waiting time to jump out from the basin characterized by γ and E_b . The convective effect is reflected by the tilt of the basin, as illustrated in Fig. 21. Under steady shear, the collective effects of thermal activation and convection are described by the SGR model. With these considerations, we can unify the values of τ_{LC} from configurations at different shear rates.

In our framework, the solid-liquid duality, which is based on the grouping of slow/fast particles, is the key to connecting τ_{LC} to rheological behaviors. Especially, this grouping is also strongly correlated to the local structure featured by terms associated with $g_{0,i}^0$ and $g_{2,i}^{-2}$, as demonstrated in Sec. IV B. Thus, it is important to examine if

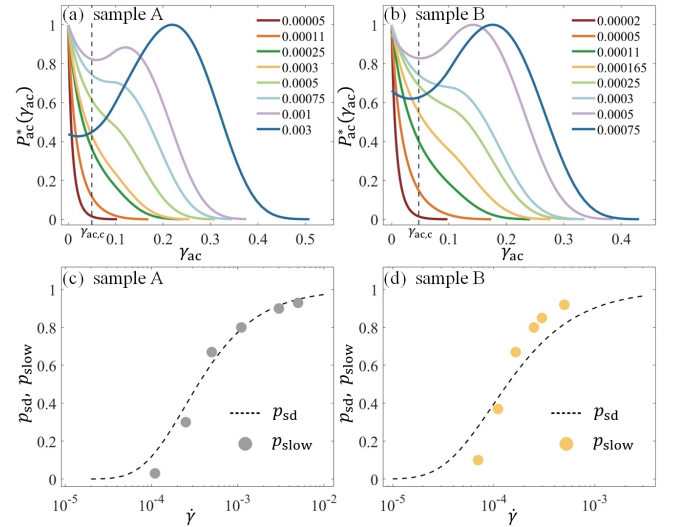


FIG. 27. (a) and (b) show $P_{ac}(\gamma_{ac})$, given by Eq. 30, at various $\dot{\gamma}$ for sample A and sample B, respectively. Here, the values of P_{ac} are scaled as $P_{ac}^*(\gamma_{ac}) = P_{ac}(\gamma_{ac})/P_{ac,max}(\gamma_{ac})$. The vertical dashed line in each panel denotes the effective range of $P_{ac}(\gamma_{ac})$ at the lowest $\dot{\gamma}$. (c) and (d) show the results of the percentage of shear-driven particles p_{sd} (dashed lines), defined by Eq. 31, at different $\dot{\gamma}$ for sample A and sample B, respectively. The results of the proportion of slow particles p_{slow} , which has been shown in Fig. 13, are replotted (symbols).

the PEL picture can give such grouping for conditions of steady shear. To explore this problem, we introduce the concept of activation strain γ_{ac} , which represents the strain at which particles jump out from the basin. Particular attention is paid to the distribution of γ_{ac} , denoted as $P_{ac}(\gamma_{ac})$. Under steady shear, $P_{ac}(\gamma_{ac})$ is given by:

$$P_{ac}(\gamma_{ac}) = \int \frac{1}{g(E_b)} e^{E(\gamma_{ac})/k_B T} P_s(\gamma_{ac}, E_b) dE_b. \quad (30)$$

Figure 27 (a) and (b) give the $P_{ac}(\gamma_{ac})$ of sample A and sample B, respectively. For the sake of clarity, we plot the scaled results $P_{ac}^*(\gamma_{ac}) = P_{ac}(\gamma_{ac})/P_{ac,max}(\gamma_{ac})$, where $P_{ac,max}(\gamma_{ac})$ is the maximum value of $P_{ac}(\gamma_{ac})$. At the lowest $\dot{\gamma}$ shown here (in the Newtonian regime), $P_{ac}(\gamma_{ac})$ is exponential-like. In Fig. 27 (a) and (b), we use vertical dashed lines to mark the effective range of $P_{ac}(\gamma_{ac})$ at the lowest $\dot{\gamma}$, denoted as $\gamma_{ac,c}$. As $\dot{\gamma}$ increases, $P_{ac}(\gamma_{ac})$ shifts to the regime of larger γ_{ac} . More importantly, $P_{ac}(\gamma_{ac})$ gradually exhibits a bimodal feature composed of an exponential-like component at small γ_{ac} regime and a gaussian-like component at large γ_{ac} regime, with the latter being enhanced by shear. The emergence of the gaussian-like component at large γ_{ac} manifests the change of the way of relaxation. For particles corresponding to the gaussian-like component, their local configurations are significantly strained by external shear before relaxation. Qualitatively, these particles are likely slow particles: Their dynamics are slower than external shear, so that there is enough time for their local

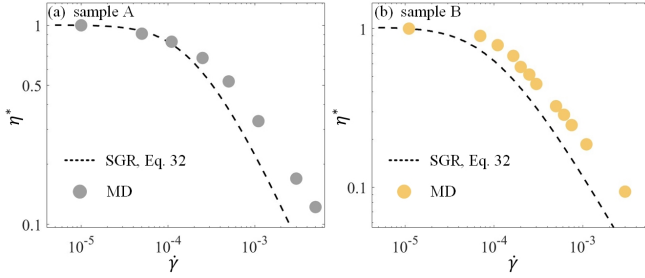


FIG. 28. Normalized shear viscosity η^* as a function of $\dot{\gamma}$. (a) and (b) show the results of sample A and sample B, respectively. Dashed lines denote the SGR results calculated with Eq. 32. Symbols denote the results found from MD data.

configurations to be strongly strained by external shear. On the contrary, remaining particles can be considered as likely fast particles, since there is not enough time for external shear to drive their local configurations to larger strains.

As seen in Fig. 27 (a) and (b), $\gamma_{ac,c}$ gives a rough boundary between the exponential-like component and the gaussian-like component. Thus, we can evaluate the percentage of the gaussian-like component as follows:

$$p_{sd} = \int_{\gamma_{ac,c}}^{\infty} P_{ac}(\gamma_{ac}) d\gamma_{ac}. \quad (31)$$

Here, the subscript “sd” denotes “shear-driven”, meaning that the local configuration and relaxation of particles corresponding to the gaussian-like component are strongly driven by shear. We plot the results of p_{sd} as a function of $\dot{\gamma}$ for two samples in Fig. 27 (c) and (d). According to the above analysis, the gaussian-like component indicates slow particles. Thus, in Fig. 27 (c) and (d), we replot the results of p_{slow} shown in Fig. 13, which is obtained from the MD data, for comparison. Their dependences on $\dot{\gamma}$ are seen to be similar. Especially, p_{sd} gradually saturates as the system enters the shear-thinning regime. The observations found in Fig. 27 suggest that the SGR model exhibits two groups of responses to shear, which captures the major feature of the grouping of slow/fast particles.

By adopting the strategy that the macroscopic stress is proportional to the average of the atomic level stress [69], we can evaluate the shear stress of the system by the stress experienced by a particle in its basin. For simplicity, this atomic level stress can be calculated by $dE(\gamma)/d\gamma$, where $E(\gamma)$ is given by Eq. 16. Therefore, under steady state, the shear stress derived from the SGR model is given by:

$$\sigma_{SGR} \sim \iint \frac{dE(\gamma)}{d\gamma} P_s(\gamma, E_b) dE_b d\gamma. \quad (32)$$

Then, the SGR viscosity can be found by $\eta_{SGR} = \sigma_{SGR}/\dot{\gamma}$. In Fig. 28, we show the results of η_{SGR} , normalized as $\eta_{SGR}^* = \eta_{SGR}/\eta_{eq}$, for two samples. $\eta_{SGR}(\dot{\gamma})$

captures the general features of shear thinning: As $\dot{\gamma}$ increases, it is able to delineate three rheological regimes, i.e., Newtonian regime, crossover regime, and shear-thinning regime. Compared with Fig. 27 (c) and (d), it can be seen that the crossover regime appears when p_{sd} becomes finite, and the shear-thinning regime appears when p_{sd} starts to saturate. This result suggests that the emergence of shear thinning is due to the increasingly dominant role of shear-driven particles in the system. The picture given by the PEL framework is consistent with our MD results shown in Sec. III.

We also plot the MD results of the normalized viscosity in Fig. 28. The SGR results and the MD results exhibit similar behaviors at the qualitative level. Nevertheless, the quantitative deviation appears and grows as $\dot{\gamma}$ increases. We will discuss about this point in the next subsection.

To briefly summarize these two subsections, we try to rationalize the MD results found in Secs. II – IV, which connect microscopic structure to macroscopic flow behaviors of supercooled liquids, within the framework of PEL. The PEL approach simplifies the intricate many-body interaction into particle-level basins. Moreover, it condenses the structural information characterized by $g_{0,i}^0$ and $g_{2,i}^{-2}$ into the height and strain characteristics of basins, enabling us to quantify the connection between local configuration and dynamics. The physical significance of τ_{LC} and τ_{sh} , and the effects of shear flow and thermal activation, are clearly illustrated in the PEL picture. With the aid of the SGR model, the relation between structure and rheology in flow state is clarified. Particularly, the model exhibits two distinct shear responses as evidenced by the bimodal distribution shown in Fig. 27 (a) and (b). The relative proportion of these two responses dictates the variation of viscosity with respect to $\dot{\gamma}$, as illustrated in Fig. 28.

C. Correlation

The systematic deviation between model results and MD results shown in Fig. 28 could be due to many reasons. For example, the basin shape $E(\gamma)$ we adopt could be oversimplified [141]; the restructuring process is ignored in the SGR model, etc. In our opinion, one of the key reasons is that the model given by Eqs. 19 – 21 ignores the correlation among the cage-jump events of different particles. In fact, it has been demonstrated that there exists an elasticity-mediated long-ranged correlation among local flow events in glasses [92, 108]. In our recent work [83], we also find the evidence of dynamic facilitation mediated by elasticity in solid-like regions in flowing supercooled liquids. In principle, as $\dot{\gamma}$ increases, such long-ranged correlation in a supercooled liquid should become more significant as the solid-like component grows. To account for this correlation while maintaining the simplicity of the model, one can replace the thermal term $k_B T$ in Eq. 19 by the effective activa-

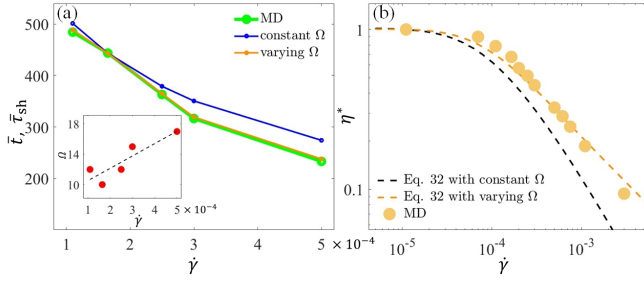


FIG. 29. (a) $\bar{\tau}_{sh}(\dot{\gamma})$ (green circles, found from MD data) and $\bar{t}(\dot{\gamma})$ (defined in Eq. 33) for sample B. Here, $\bar{t}(\dot{\gamma})$ are calculated in two ways: with constant Ω (blue points) and with varying Ω determined by Eq. 34 (orange points). Inset: the varying Ω (red circles), determined by Eq. 34, as a function of $\dot{\gamma}$. The dashed line denotes the linear fit of Ω with respect to $\dot{\gamma}$. (b) Normalized viscosity of sample B. Symbols denote the MD result. Black dashed line denotes the result calculated with Eq. 32 with constant Ω . This result has been shown in Fig. 28 (b). Orange dashed line denotes the result calculated with the varying Ω shown in the inset of (a).

tion temperature x [23]. Although the use of an effective temperature to describe the effect of mechanical noise has been questioned [142], it can qualitatively capture the phenomenon that the correlation among particles can facilitate the relaxation of a region.

Here, we tentatively adopt a more straightforward approach to phenomenologically incorporate this correlation. In the preceding two subsections, the activation volume Ω is set to the volume of a cage and is assumed to be constant with respect to $\dot{\gamma}$. This assumption is inconsistent with the long-ranged feature of the elasticity-mediated correlation in solid-like regions and the growth of the solid-like component with $\dot{\gamma}$. To explicitly account for this correlation, we assume that Ω increases correspondingly with $\dot{\gamma}$.

We use the following strategy to determine Ω . In Sec. V A, we introduce $\bar{t}(E_b, \dot{\gamma})$ in Eq. 18 to represent τ_{sh} in the start-up shear. The results are shown in Fig. 23. It is seen that the values of τ_{sh} evaluated by $\bar{t}(E_b, \dot{\gamma})$ and those measured from MD data have small but non-negligible discrepancy. Thus, we can determine a reasonable Ω by minimizing the difference between $\bar{t}(E_b, \dot{\gamma})$ and τ_{sh} for each $\dot{\gamma}$. To be specific, we introduce the basin-averaged $\bar{t}(E_b, \dot{\gamma})$, denoted as $\bar{t}(\dot{\gamma})$:

$$\bar{t}(\dot{\gamma}) = \int P_b(E_b) \bar{t}(E_b, \dot{\gamma}) dE_b. \quad (33)$$

Conceptually, $\bar{t}(\dot{\gamma})$ corresponds to the globally averaged τ_{sh} , denoted as $\bar{\tau}_{sh}(\dot{\gamma})$. The value of $\bar{t}(\dot{\gamma})$ depends on Ω . Therefore, we can perform the following minimization by adjusting the value of Ω for each $\dot{\gamma}$:

$$\min_{\Omega} |\bar{\tau}_{sh}(\dot{\gamma}) - \bar{t}(\dot{\gamma})|. \quad (34)$$

In Fig. 29 (a), we present $\bar{\tau}_{sh}(\dot{\gamma})$ and $\bar{t}(\dot{\gamma})$ using sample B as an illustrative example. Here, $\bar{t}(\dot{\gamma})$ is computed

with two ways: the blue symbols give the result calculated with a constant Ω ; the orange symbols give the result calculated with the $\dot{\gamma}$ -dependent Ω determined by Eq. 34. Generally speaking, incorporating a constant Ω leads to an over-estimation of τ_{sh} at large $\dot{\gamma}$. In the inset of Fig. 29 (a), we give the result of $\Omega(\dot{\gamma})$ determined by Eq. 34 for sample B. $\Omega(\dot{\gamma})$ displays an increasing trend with $\dot{\gamma}$, corresponding to the enhancement of the correlation among flow events due to the increasingly dominant role of solid-like regions as $\dot{\gamma}$ increases. Within the mean-field framework of SGR, the increment of $\Omega(\dot{\gamma})$ can be understood by the enhancement of the rigidity [143]. As the system becomes more rigid, the relaxation of the central particle will influence more surrounding particles, resulting in a larger Ω [15, 80].

By replacing the constant Ω in Eq. 32 with $\Omega(\dot{\gamma})$, we recalculate the viscosity, and plot the result in Fig. 29 (b). We also replot the MD result and the result calculated by Eq. 32 with the constant Ω , which have been shown in Fig. 28 (b). It is seen that by using $\Omega(\dot{\gamma})$, the agreement between MD result and model result is significantly improved.

VI. CONCLUDING REMARKS

How do supercooled liquids flow? From the macroscopic viewpoint, Maxwell has laid the foundation for understanding the mechanical response of viscoelastic matter, including supercooled liquids, by introducing the Maxwell time τ_M and the solid-liquid duality associated with τ_M . This approach, though extremely important in concept, lacks a clear molecular basis, which impedes the construction of a more general theory from microscopic structure and interaction. At the microscopic level, DH is one of the most important dynamical characteristics of supercooled liquids. Particularly, it has been proven that DH is closely correlated to the zero-shear viscosity [15]. Knowing these facts, one may expect a microscopic approach, which embodies the conceptual solid-liquid duality by involving DH, for elucidating the flow behaviors of supercooled liquids.

The key to bridging the gap between the microscopic and the macroscopic worlds is the local configurational relaxation time τ_{LC} . Defined at the particle level, τ_{LC} well reflects the local mobility and the heterogeneous feature of dynamics. Moreover, τ_{LC} plays a role similar to that of τ_M in the Maxwell model: Depending on the comparison between τ_{LC} and the external driving rate, the corresponding local region can exhibit solid-like or liquid-like response. Then, the macroscopic behavior is given by the average behavior of all local regions in the system. These results unify the concept of solid-liquid duality and DH into a micro-mechanical picture for the flow of supercooled liquids. τ_{LC} has an unambiguous structural foundation. With the aid of statistical learning methods and PEL, we show that τ_{LC} is mainly determined by the combined effect of local packing and local configurational dis-

tortion, which are respectively represented by the barrier height and the tilted strain of the particle-level energy basin. With these efforts, we establish a chain relation of *local configuration* – *local dynamics* – *local response* – *flow behaviors* for supercooled liquids.

Finally, we would like to point out that supercooled liquids are highly diverse, manifested by distinct kinds of microscopic interactions and dynamical characteristics [144]. For example, water, interacting by hydrogen bonding, exhibits two liquid phases when entering the supercooled state [145–150]. How these two phases respond to external shear, and how external shear affects these two phases, could be important for quantifying the nonlinear rheology of water [151, 152]. Another example is the gaussian-core liquid [153]. It belongs to ultrasoft liquids, which are featured by a very soft core in the interparticle interaction and represent a wide variety of soft materials [154, 155]. The supercooled gaussian-core liquid behaves as a mean-field fluid [156] and exhibits much weaker heterogeneity in dynamics compared with other model supercooled liquids [157], while maintaining an evident shear thinning [98]. In this case, the role of DH, as well as the related structural features, in determining the rheology could be different. Note that, the method based on τ_{LC} proposed here is also applicable to other systems. Such efforts could be helpful for achieving a more general framework for understanding the flow of supercooled liquids.

ACKNOWLEDGMENTS

This research was partially supported by the National Natural Science Foundation of China (no. 11975136). The authors acknowledge the Center of High Performance Computing, Tsinghua University for providing computational resources and Dr. Dejie Kong for his help in Sec. IV.

Appendix A: CIRCLING CLUSTERS

In this part, we introduce the approach for partitioning slow and fast particles into clusters. As an exemplary illustration, we elaborate on the process of partitioning the slow particles. The similar procedure can be applied to fast particles.

As seen from Fig. 2, the clusters of slow particles exhibit hierarchical characteristics. Thus, it can be imagined that slow particles “grow” from different slow centers and form different slow clusters. Consequently, we can partition the particles based on the spatial positions of the slow centers. The identification of slow centers is carried out using the “Grids” method. In brief, the simulation box is divided into small cubic grids. The side length of each grid is $L/20$, where L is the length of the simulation box. Subsequently, with the following expression, each grid undergoes a convolution with particles’

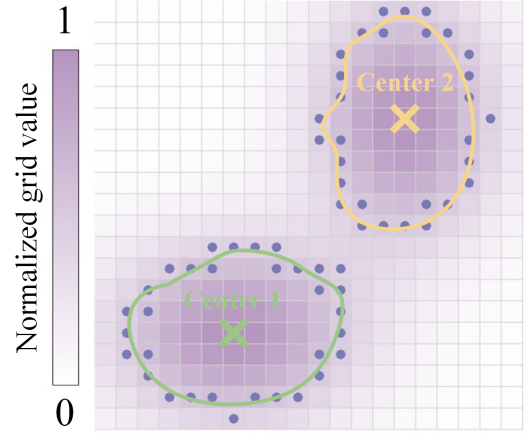


FIG. 30. Illustration of the “Grids” method for identification of slow/fast clusters. Here, the system is divided into grids. Each grid is assigned a value, which can be τ_{LC} or other variables. Without loss of generality, the values of the grids are normalized to the range of 0 to 1. Giving a typical example, we define the regions of interest as those grids whose values are greater than 0.5. The boundaries of these regions can be identified. Here, we use points to represent the boundaries. Our objective is to divide the regions of interest into clusters. First, we identify the center grids. A center grid is defined as the grid whose value is greater than those of all its neighboring grids. In this figure, cross symbols are used to denote the centers. Subsequently, each grid within the region of interest is assigned to the nearest center grid. As a result, each center grid has its “jurisdiction area”, which is represented by solid lines in the figure.

τ_{LC} , yielding a value denoted as g :

$$g_i = \frac{\sum_j \tau_{LC,j} \exp(-r_{ij}/l_{cg})}{\sum_j \exp(-r_{ij}/l_{cg})}, \quad (A1)$$

where the subscript “ i ” denotes the i th grid, $\tau_{LC,j}$ is the τ_{LC} of particle j , r_{ij} is the distance between particle j and grid i , and l_{cg} is a characteristic length employed in the convolution and is set to $L/20$. The summations in Eq. A1 are performed over all particles.

We define slow centers as the grids whose g values are greater than those of their 26 neighboring grids. This criterion guarantees that the slow centers are identified as local maxima. By utilizing these slow centers, each slow particle is assigned to the nearest center, thereby enabling the division of all slow particles into distinct clusters. The schematic diagram of this method is presented in Fig. 30.

Appendix B: EFFECTIVE MODULUS OF LER

In this part, we give the method for evaluating the effective modulus of LER from neighbor loss process. We first calculate the bond-breaking correlation function $C_i(t)$ for particle i [43, 67] as $C_i(t) = n_i(t|0)/n_i(0)$, where

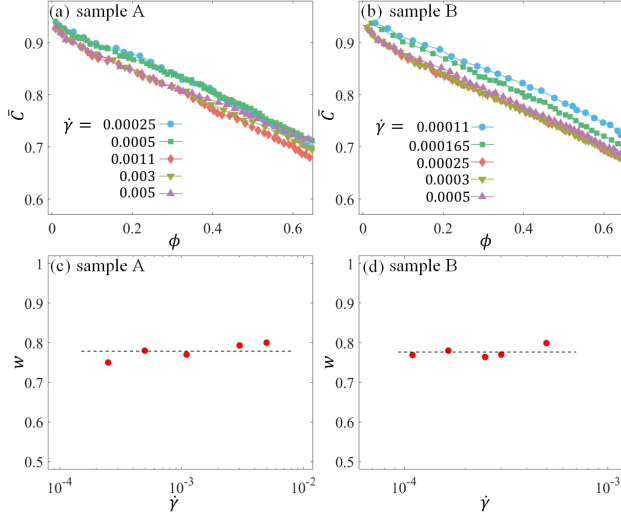


FIG. 31. (a) and (b) show the relation between the average neighbor-keeping ratio among slow particles, denoted as \bar{C} , and the ratio of particles that have experienced cage jump in the system, denoted as ϕ , for sample A and sample B, respectively, at various $\dot{\gamma}$. (c) and (d) show the results of w (symbols), found from Eq. B3, as a function of $\dot{\gamma}$ for sample A and sample B, respectively. In (c) and (d), horizontal dashed lines denote the mean values of w averaged over all $\dot{\gamma}$ for sample A and sample B.

$n_i(0)$ is the initial number of neighbors of particle i at a given time origin, and $n_i(t|0)$ is the number of these initial neighbors that remain neighbors of particle i after a time interval t . Here, a particle is considered a neighbor of a reference particle if the distance between them is within the first minimum of the pair distribution function $g(r)$. Inspired by Refs. [71, 97] we posit that the modulus decays to 0 for a given region when, on average, half of the neighboring particles for particles within this region are lost. Furthermore, we assume that the change of modulus is approximately proportional to the average change in the number of neighbors. Then, we have:

$$G(t) \approx G_{\text{ini}} \frac{\bar{C}(t) - 0.5}{0.5}, \quad (\text{B1})$$

where $\bar{C}(t)$ is the averaged $C_i(t)$ for a given region. $\bar{C}(t)$ is closely related to the percentage of jump $\phi(t)$, which represents the portion of particles that have undergone cage jump by time t in a given region. Figure 31 (a) and (b) exhibit the relation between $\bar{C}(t)$ of slow particles and $\phi(t)$ of the whole system for sample A and sample B, respectively, at several $\dot{\gamma}$. It is seen that $\bar{C}(t)$ and $\phi(t)$ are nearly linearly related, and their relation is not very sensitive to $\dot{\gamma}$ and sample. With these results, we can find $G(t)$, and the maximum stress accumulated within the elastic stage of LER is written as:

$$\sigma_{\text{el}} = \int_0^{\tau_{\text{el}}} G(t) \dot{\gamma} dt. \quad (\text{B2})$$

TABLE I. The 15 important features for two samples.

Rank	sample A				sample B			
	gen ^a	l	m	r	gen ^a	l	m	r
1	2	0	0	1.3	2	0	0	1.3
2	2	2	-2	0.9	2	2	-2	1.2
3	2	0	0	1.1	2	0	0	1.4
4	2	0	0	1.2	2	0	0	0.9
5	2	0	0	3.0	2	0	0	1.2
6	0	0	0	1.0	1	2	-2	1.2
7	1	2	-2	0.9	1	0	0	1.4
8	2	0	0	0.8	2	0	0	1.1
9	2	0	0	1.9	2	0	0	2.3
10	2	0	0	1.4	0	0	0	1.3
11	2	0	0	0.7	2	0	0	2.1
12	2	0	0	1.1	2	0	0	3.4
13	2	2	-2	2.9	2	0	0	1.5
14	2	0	0	1.7	2	0	0	0.8
15	2	0	0	1.6	0	2	-2	5.0

^a “gen” denotes the generation of the feature.

The effective modulus G_{eff} is defined by $\sigma_{\text{el}} = G_{\text{eff}} \dot{\gamma} \tau_{\text{el}}$. Thus, we have:

$$G_{\text{eff}} = w G_{\text{ini}} = \frac{1}{\tau_{\text{el}}} \int_0^{\tau_{\text{el}}} G(t) dt \approx \frac{G_{\text{ini}}}{\tau_{\text{el}}} \int_0^{\tau_{\text{el}}} \frac{\bar{C}(t) - 0.5}{0.5} dt. \quad (\text{B3})$$

The values of w obtained by the preceding equation for sample A and sample B are given in Fig. 31 (c) and (d), respectively.

Appendix C: IMPORTANCE OF STRUCTURAL FEATURES

Once the N_X -dimensional feature vector X for each particle has been computed, it is insightful to investigate the contribution of each element in X to the final correlation. Thus, one can rank the N_X elements in X based on their importance.

Firstly, we directly compute the correlation coefficient between each element in X and the target property. The element with the maximum correlation is denoted as F_1 . Clearly, we should extend F_1 to include more elements to capture a more comprehensive relationship. To determine the second most important element, F_2 , we adopt a method of exhaustion. Specifically, we combine F_1 with each of the remaining elements in X to form $N_X - 1$ two-element vectors. For each two-element vector, we use a linear regression model to establish the correlation between this vector and the target property, and record the correlation coefficient. This operation results in a list of correlation coefficients, each corresponding to a different two-element vector. The maximum correlation coefficient in this list is identified, and the corresponding two-element vector, which has the highest correlation, is noted. The second element in this vector is designated as F_2 .

Based on F_1 and F_2 , we can search for the third most important element, F_3 . The method is similar to the one used to determine F_2 . Specifically, we exhaustively combine each of the remaining $N_X - 2$ elements with F_1 and F_2 to form three-element vectors. For each three-element vector, we compute the correlation coefficient

and identify the best combination. The third element in the best combination is designated as F_3 . By following this routine, we can subsequently determine F_4 , F_5 , and so on.

Table I lists the top 15 most important features for two samples.

-
- [1] J. C. Maxwell, IV. On the dynamical theory of gases, *Philosophical Transactions of the Royal Society of London* **157**, 49 (1867).
 - [2] P. Oswald, *Rheophysics: The Deformation and Flow of Matter* (Cambridge University Press, Cambridge ; New York, 2009).
 - [3] R. G. Larson, *Constitutive Equations for Polymer Melts and Solutions*, Butterworths Series in Chemical Engineering (Butterworths, Boston, 1988).
 - [4] S. F. Edwards, The statistical mechanics of polymerized material, *Proceedings of the Physical Society* **92**, 9 (1967).
 - [5] P. G. De Gennes, Reptation of a Polymer Chain in the Presence of Fixed Obstacles, *The Journal of Chemical Physics* **55**, 572 (1971).
 - [6] M. Doi and S. F. Edwards, *The Theory of Polymer Dynamics*, International Series of Monographs on Physics (Clarendon press, Oxford, 1986).
 - [7] G. Marrucci, Dynamics of entanglements: A nonlinear model consistent with the Cox-Merz rule, *Journal of Non-Newtonian Fluid Mechanics* **62**, 279 (1996).
 - [8] D. W. Mead, R. G. Larson, and M. Doi, A Molecular Theory for Fast Flows of Entangled Polymers, *Macromolecules* **31**, 7895 (1998).
 - [9] R. S. Graham, A. E. Likhtman, T. C. B. McLeish, and S. T. Milner, Microscopic theory of linear, entangled polymer chains under rapid deformation including chain stretch and convective constraint release, *Journal of Rheology* **47**, 1171 (2003).
 - [10] J.-P. Hansen and I. R. McDonald, *Theory of Simple Liquids: With Applications to Soft Matter*, 4th ed. (Elsevier/AP, Amstersdam, 2013).
 - [11] T. Voigtmann, Nonlinear glassy rheology, *Current Opinion in Colloid & Interface Science* **19**, 549 (2014).
 - [12] W. E. Alley, B. J. Alder, and S. Yip, The neutron scattering function for hard spheres, *Physical Review A* **27**, 3174 (1983).
 - [13] W. Schirmacher, G. Ruocco, and V. Mazzone, Heterogeneous Viscoelasticity: A Combined Theory of Dynamic and Elastic Heterogeneity, *Physical Review Letters* **115**, 015901 (2015).
 - [14] M. D. Ediger, Spatially Heterogeneous Dynamics in Supercooled Liquids, *Annual Review of Physical Chemistry* **51**, 99 (2000).
 - [15] A. Cavagna, Supercooled liquids for pedestrians, *Physics Reports* **476**, 51 (2009).
 - [16] G. L. Hunter and E. R. Weeks, The physics of the colloidal glass transition, *Reports on Progress in Physics* **75**, 066501 (2012).
 - [17] N. Lačević, F. W. Starr, T. B. Schröder, and S. C. Glotzer, Spatially heterogeneous dynamics investigated via a time-dependent four-point density correlation function, *The Journal of Chemical Physics* **119**, 7372 (2003).
 - [18] L. Wang, N. Xu, W. H. Wang, and P. Guan, Revealing the Link between Structural Relaxation and Dynamic Heterogeneity in Glass-Forming Liquids, *Physical Review Letters* **120**, 125502 (2018).
 - [19] A. Furukawa and H. Tanaka, Direct evidence of heterogeneous mechanical relaxation in supercooled liquids, *Physical Review E* **84**, 061503 (2011).
 - [20] S. Chakrabarty, I. Tah, S. Karmakar, and C. Dasgupta, Block Analysis for the Calculation of Dynamic and Static Length Scales in Glass-Forming Liquids, *Physical Review Letters* **119**, 205502 (2017).
 - [21] B. Shang, J. Rottler, P. Guan, and J.-L. Barrat, Local versus Global Stretched Mechanical Response in a Supercooled Liquid near the Glass Transition, *Physical Review Letters* **122**, 105501 (2019).
 - [22] L. Berthier, Self-Induced Heterogeneity in Deeply Supercooled Liquids, *Physical Review Letters* **127**, 088002 (2021).
 - [23] P. Sollich, F. Lequeux, P. Hébraud, and M. E. Cates, Rheology of Soft Glassy Materials, *Physical Review Letters* **78**, 2020 (1997).
 - [24] A. Widmer-Cooper and P. Harrowell, Predicting the Long-Time Dynamic Heterogeneity in a Supercooled Liquid on the Basis of Short-Time Heterogeneities, *Physical Review Letters* **96**, 185701 (2006).
 - [25] A. Widmer-Cooper, H. Perry, P. Harrowell, and D. R. Reichman, Irreversible reorganization in a supercooled liquid originates from localized soft modes, *Nature Physics* **4**, 711 (2008).
 - [26] S. S. Schoenholz, E. D. Cubuk, D. M. Sussman, E. Kaxiras, and A. J. Liu, A structural approach to relaxation in glassy liquids, *Nature Physics* **12**, 469 (2016).
 - [27] X. Ma, Z. S. Davidson, T. Still, R. J. S. Ivancic, S. S. Schoenholz, A. J. Liu, and A. G. Yodh, Heterogeneous Activation, Local Structure, and Softness in Supercooled Colloidal Liquids, *Physical Review Letters* **122**, 028001 (2019).
 - [28] E. D. Cubuk, S. S. Schoenholz, J. M. Rieser, B. D. Malone, J. Rottler, D. J. Durian, E. Kaxiras, and A. J. Liu, Identifying Structural Flow Defects in Disordered Solids Using Machine-Learning Methods, *Physical Review Letters* **114**, 108001 (2015).
 - [29] H. Tong and H. Tanaka, Revealing Hidden Structural Order Controlling Both Fast and Slow Glassy Dynamics in Supercooled Liquids, *Physical Review X* **8**, 011041 (2018).
 - [30] M. Lerbinger, A. Barbot, D. Vandembroucq, and S. Patinet, Relevance of Shear Transformations in the Relaxation of Supercooled Liquids, *Physical Review Letters* **129**, 195501 (2022).
 - [31] S. Patinet, D. Vandembroucq, and M. L. Falk, Connecting Local Yield Stresses with Plastic Activity in

- Amorphous Solids, *Physical Review Letters* **117**, 045501 (2016).
- [32] D. Richard, M. Ozawa, S. Patinet, E. Stanifer, B. Shang, S. A. Ridout, B. Xu, G. Zhang, P. K. Morse, J.-L. Barrat, L. Berthier, M. L. Falk, P. Guan, A. J. Liu, K. Martens, S. Sastry, D. Vandembroucq, E. Lerner, and M. L. Manning, Predicting plasticity in disordered solids from structural indicators, *Physical Review Materials* **4**, 113609 (2020).
 - [33] V. Bapst, T. Keck, A. Grabska-Barwińska, C. Donner, E. D. Cubuk, S. S. Schoenholz, A. Obika, A. W. R. Nelson, T. Back, D. Hassabis, and P. Kohli, Unveiling the predictive power of static structure in glassy systems, *Nature Physics* **16**, 448 (2020).
 - [34] E. Boattini, F. Smallenburg, and L. Filion, Averaging Local Structure to Predict the Dynamic Propensity in Supercooled Liquids, *Physical Review Letters* **127**, 088007 (2021).
 - [35] Y. Xia, X. Yang, J. Huang, R. Liu, N. Xu, M. Yang, and K. Chen, Orientational Order in Dense Colloidal Liquids and Glasses, *Physical Review Letters* **131**, 128201 (2023).
 - [36] H. Zhang, Q. Zhang, F. Liu, and Y. Han, Anisotropic-Isotropic Transition of Cages at the Glass Transition, *Physical Review Letters* **132**, 078201 (2024).
 - [37] A. Malins, S. R. Williams, J. Eggers, and C. P. Royall, Identification of structure in condensed matter with the topological cluster classification, *The Journal of Chemical Physics* **139**, 234506 (2013).
 - [38] R. G. Larson, *The Structure and Rheology of Complex Fluids*, Topics in Chemical Engineering (Oxford university press, New York, 1999).
 - [39] J. R. Seth, L. Mohan, C. Locatelli-Champagne, M. Cloitre, and R. T. Bonnecaze, A micromechanical model to predict the flow of soft particle glasses, *Nature Materials* **10**, 838 (2011).
 - [40] D. Vlassopoulos and M. Cloitre, Tunable rheology of dense soft deformable colloids, *Current Opinion in Colloid & Interface Science* **19**, 561 (2014).
 - [41] J. Huang, J. O. Cochran, S. M. Fielding, M. C. Marchetti, and D. Bi, Shear-Driven Solidification and Nonlinear Elasticity in Epithelial Tissues, *Physical Review Letters* **128**, 178001 (2022).
 - [42] D. Kong, W.-R. Chen, K.-Q. Zeng, L. Porcar, and Z. Wang, Localized Elasticity Governs the Nonlinear Rheology of Colloidal Supercooled Liquids, *Physical Review X* **12**, 041006 (2022).
 - [43] R. Yamamoto and A. Onuki, Dynamics of highly supercooled liquids: Heterogeneity, rheology, and diffusion, *Physical Review E* **58**, 3515 (1998).
 - [44] C. P. Royall and S. R. Williams, The role of local structure in dynamical arrest, *Physics Reports* **560**, 1 (2015).
 - [45] H. Tanaka, H. Tong, R. Shi, and J. Russo, Revealing key structural features hidden in liquids and glasses, *Nature Reviews Physics* **1**, 333 (2019).
 - [46] S. Karmakar, C. Dasgupta, and S. Sastry, Length scales in glass-forming liquids and related systems: A review, *Reports on Progress in Physics* **79**, 016601 (2016).
 - [47] A. Heuer, Exploring the potential energy landscape of glass-forming systems: From inherent structures via metabasins to macroscopic transport, *Journal of Physics: Condensed Matter* **20**, 373101 (2008).
 - [48] F. Sciortino, Potential energy landscape description of supercooled liquids and glasses, *Journal of Statistical Mechanics: Theory and Experiment* **2005**, P05015 (2005).
 - [49] S. Sastry, P. G. Debenedetti, and F. H. Stillinger, Signatures of distinct dynamical regimes in the energy landscape of a glass-forming liquid, *Nature* **393**, 554 (1998).
 - [50] D. L. Malandro and D. J. Lacks, Relationships of shear-induced changes in the potential energy landscape to the mechanical properties of ductile glasses, *The Journal of Chemical Physics* **110**, 4593 (1999).
 - [51] W. Kob and H. C. Andersen, Testing mode-coupling theory for a supercooled binary Lennard-Jones mixture I: The van Hove correlation function, *Physical Review E* **51**, 4626 (1995).
 - [52] M. P. Allen and D. J. Tildesley, *Computer Simulation of Liquids*, second edition ed. (Oxford University Press, Oxford, 2017).
 - [53] A. W. Lees and S. F. Edwards, The computer study of transport processes under extreme conditions, *Journal of Physics C: Solid State Physics* **5**, 1921 (1972).
 - [54] D. J. Evans and G. P. Morriss, Nonlinear-response theory for steady planar Couette flow, *Physical Review A* **30**, 1528 (1984).
 - [55] A. P. Thompson, H. M. Aktulga, R. Berger, D. S. Bolintineanu, W. M. Brown, P. S. Crozier, P. J. In 't Veld, A. Kohlmeyer, S. G. Moore, T. D. Nguyen, R. Shan, M. J. Stevens, J. Tranchida, C. Trott, and S. J. Plimpton, LAMMPS - a flexible simulation tool for particle-based materials modeling at the atomic, meso, and continuum scales, *Computer Physics Communications* **271**, 108171 (2022).
 - [56] W. Gotze and L. Sjogren, Relaxation processes in supercooled liquids, *Reports on Progress in Physics* **55**, 241 (1992).
 - [57] Y. Chen, Z. Ye, K. Wang, J. Huang, H. Tong, Y. Jin, K. Chen, H. Tanaka, and P. Tan, Visualizing slow internal relaxations in a two-dimensional glassy system, *Nature Physics* **19**, 969 (2023).
 - [58] T. B. Schröder, S. Sastry, J. C. Dyre, and S. C. Glotzer, Crossover to potential energy landscape dominated dynamics in a model glass-forming liquid, *The Journal of Chemical Physics* **112**, 9834 (2000).
 - [59] R. Candelier, O. Dauchot, and G. Biroli, Building Blocks of Dynamical Heterogeneities in Dense Granular Media, *Physical Review Letters* **102**, 088001 (2009).
 - [60] R. Candelier, A. Widmer-Cooper, J. K. Kummerfeld, O. Dauchot, G. Biroli, P. Harrowell, and D. R. Reichman, Spatiotemporal Hierarchy of Relaxation Events, Dynamical Heterogeneities, and Structural Reorganization in a Supercooled Liquid, *Physical Review Letters* **105**, 135702 (2010).
 - [61] Y. Jung, J. P. Garrahan, and D. Chandler, Dynamical exchanges in facilitated models of supercooled liquids, *The Journal of Chemical Physics* **123**, 084509 (2005).
 - [62] R. Pastore, T. Kikutsuji, F. Rusciano, N. Matubayasi, K. Kim, and F. Greco, Breakdown of the Stokes-Einstein relation in supercooled liquids: A cage-jump perspective, *The Journal of Chemical Physics* **155**, 114503 (2021).
 - [63] A. Widmer-Cooper, P. Harrowell, and H. Fynewever, How Reproducible Are Dynamic Heterogeneities in a Supercooled Liquid?, *Physical Review Letters* **93**, 135701 (2004).
 - [64] E. R. Weeks, J. C. Crocker, A. C. Levitt, A. Schofield, and D. A. Weitz, Three-Dimensional Direct Imaging of

- Structural Relaxation Near the Colloidal Glass Transition, *Science* **287**, 627 (2000).
- [65] A. R. Jacob, A. S. Poulos, S. Kim, J. Vermant, and G. Petekidis, Convective Cage Release in Model Colloidal Glasses, *Physical Review Letters* **115**, 218301 (2015).
- [66] A. S. Keys, L. O. Hedges, J. P. Garrahan, S. C. Glotzer, and D. Chandler, Excitations Are Localized and Relaxation Is Hierarchical in Glass-Forming Liquids, *Physical Review X* **1**, 021013 (2011).
- [67] C. Scalliet, B. Guiselin, and L. Berthier, Thirty Milliseconds in the Life of a Supercooled Liquid, *Physical Review X* **12**, 041028 (2022).
- [68] C. Herrero and L. Berthier, Direct Numerical Analysis of Dynamic Facilitation in Glass-Forming Liquids, *Physical Review Letters* **132**, 258201 (2024).
- [69] T. Egami, Atomic level stresses, *Progress in Materials Science* **56**, 637 (2011).
- [70] N. Koumakis, M. Laurati, S. U. Egelhaaf, J. F. Brady, and G. Petekidis, Yielding of Hard-Sphere Glasses during Start-Up Shear, *Physical Review Letters* **108**, 098303 (2012).
- [71] M. Laurati, P. Maßhoff, K. J. Mutch, S. U. Egelhaaf, and A. Zaccone, Long-Lived Neighbors Determine the Rheological Response of Glasses, *Physical Review Letters* **118**, 018002 (2017).
- [72] F. Westermeier, D. Pennicard, H. Hirsemann, U. H. Wagner, C. Rau, H. Graafsma, P. Schall, M. Paul Lettinga, and B. Struth, Connecting structure, dynamics and viscosity in sheared soft colloidal liquids: A medley of anisotropic fluctuations, *Soft Matter* **12**, 171 (2016).
- [73] Z. Wang, C. N. Lam, W.-R. Chen, W. Wang, J. Liu, Y. Liu, L. Porcar, C. B. Stanley, Z. Zhao, K. Hong, and Y. Wang, Fingerprinting Molecular Relaxation in Deformed Polymers, *Physical Review X* **7**, 031003 (2017).
- [74] R. Besseling, E. R. Weeks, A. B. Schofield, and W. C. K. Poon, Three-Dimensional Imaging of Colloidal Glasses under Steady Shear, *Physical Review Letters* **99**, 028301 (2007).
- [75] V. Chikkadi and P. Schall, Nonaffine measures of particle displacements in sheared colloidal glasses, *Physical Review E* **85**, 031402 (2012).
- [76] A. Furukawa, K. Kim, S. Saito, and H. Tanaka, Anisotropic cooperative structural rearrangements in sheared supercooled liquids, *Phys. Rev. Lett.* **102**, 016001 (2009).
- [77] J. Zausch and J. Horbach, The build-up and relaxation of stresses in a glass-forming soft-sphere mixture under shear: A computer simulation study, *EPL (Europhysics Letters)* **88**, 60001 (2009).
- [78] T. Iwashita and T. Egami, Atomic mechanism of flow in simple liquids under shear, *Physical Review Letters* **108**, 196001 (2012).
- [79] J. C. Dyre, Solidity of viscous liquids, *Phys. Rev. E* **59**, 2458 (1999).
- [80] J. C. Dyre, Colloquium: The glass transition and elastic models of glass-forming liquids, *Rev. Mod. Phys.* **78**, 953 (2006).
- [81] J. C. Dyre, *Solid-That-Flows* Picture of Glass-Forming Liquids, *The Journal of Physical Chemistry Letters* **15**, 1603 (2024).
- [82] J. Chattoraj and A. Lemaître, Elastic Signature of Flow Events in Supercooled Liquids Under Shear, *Physical Review Letters* **111**, 066001 (2013).
- [83] K.-Q. Zeng, D.-X. Yu, and Z. Wang, Connecting shear thinning and dynamic heterogeneity in supercooled liquids by localized elasticity (2025), [arXiv:2501.02437v2 \[cond-mat.soft\]](https://arxiv.org/abs/2501.02437v2).
- [84] D. Richard, G. Kapteijns, J. A. Giannini, M. L. Manning, and E. Lerner, Simple and Broadly Applicable Definition of Shear Transformation Zones, *Physical Review Letters* **126**, 015501 (2021).
- [85] A. Argon, Plastic deformation in metallic glasses, *Acta Metallurgica* **27**, 47 (1979).
- [86] M. L. Falk and J. S. Langer, Dynamics of viscoplastic deformation in amorphous solids, *Physical Review E* **57**, 7192 (1998).
- [87] Y. Fan, T. Iwashita, and T. Egami, How thermally activated deformation starts in metallic glass, *Nature Communications* **5**, 5083 (2014).
- [88] P. Schall, D. A. Weitz, and F. Spaepen, Structural Rearrangements That Govern Flow in Colloidal Glasses, *Science* **318**, 1895 (2007).
- [89] L. Berthier and J.-L. Barrat, Nonequilibrium dynamics and fluctuation-dissipation relation in a sheared fluid, *The Journal of Chemical Physics* **116**, 6228 (2002).
- [90] L. Berthier, J.-L. Barrat, and J. Kurchan, A two-time-scale, two-temperature scenario for nonlinear rheology, *Phys. Rev. E* **61**, 5464 (2000).
- [91] T. Iwashita, D. M. Nicholson, and T. Egami, Elementary Excitations and Crossover Phenomenon in Liquids, *Physical Review Letters* **110**, 205504 (2013).
- [92] A. Nicolas, E. E. Ferrero, K. Martens, and J.-L. Barrat, Deformation and flow of amorphous solids: Insights from elastoplastic models, *Reviews of Modern Physics* **90**, 045006 (2018).
- [93] M. Ozawa and G. Biroli, Elasticity, Facilitation, and Dynamic Heterogeneity in Glass-Forming Liquids, *Physical Review Letters* **130**, 138201 (2023).
- [94] A. Lemaître, Structural Relaxation is a Scale-Free Process, *Physical Review Letters* **113**, 245702 (2014).
- [95] M. L. Manning and A. J. Liu, Vibrational Modes Identify Soft Spots in a Sheared Disordered Packing, *Physical Review Letters* **107**, 108302 (2011).
- [96] M. M. Cross, Rheology of non-Newtonian fluids: A new flow equation for pseudoplastic systems, *Journal of Colloid Science* **20**, 417 (1965).
- [97] A. Zaccone, P. Schall, and E. M. Terentjev, Microscopic origin of nonlinear nonaffine deformation in bulk metallic glasses, *Physical Review B* **90**, 140203 (2014).
- [98] H. Mizuno, A. Ikeda, T. Kawasaki, and K. Miyazaki, Universal mechanism of shear thinning in supercooled liquids, *Communications Physics* **7**, 199 (2024).
- [99] Sharon L. Webb and Donald B. Dingwell, The onset of non-Newtonian rheology of silicate melts: A fiber elongation study, *Physics and Chemistry of Minerals* **17**, 10.1007/BF00199663 (1990).
- [100] M. Fuchs and M. E. Cates, Theory of nonlinear rheology and yielding of dense colloidal suspensions, *Phys. Rev. Lett.* **89**, 248304 (2002).
- [101] K. Miyazaki and D. R. Reichman, Molecular hydrodynamic theory of supercooled liquids and colloidal suspensions under shear, *Phys. Rev. E* **66**, 050501 (2002).
- [102] J. M. Brader, T. Voigtmann, M. Fuchs, R. G. Larson, and M. E. Cates, Glass rheology: From mode-coupling theory to a dynamical yield criterion, *Proceedings of the National Academy of Sciences* **106**, 15186–15191 (2009).
- [103] D. Bonn, M. M. Denn, L. Berthier, T. Divoux, and

- S. Manneville, Yield stress materials in soft condensed matter, *Reviews of Modern Physics* **89**, 035005 (2017).
- [104] I. Fuereeder and P. Ilg, Transient inhomogeneous flow patterns in supercooled liquids under shear, *Soft Matter* **13**, 2192 (2017).
- [105] C. Liu, S. Dutta, P. Chaudhuri, and K. Martens, Elastoplastic Approach Based on Microscopic Insights for the Steady State and Transient Dynamics of Sheared Disordered Solids, *Physical Review Letters* **126**, 138005 (2021).
- [106] S. Rossi, G. Biroli, M. Ozawa, G. Tarjus, and F. Zamponi, Finite-Disorder Critical Point in the Yielding Transition of Elastoplastic Models, *Physical Review Letters* **129**, 228002 (2022).
- [107] H. J. Barlow, J. O. Cochran, and S. M. Fielding, Ductile and Brittle Yielding in Thermal and Athermal Amorphous Materials, *Physical Review Letters* **125**, 168003 (2020).
- [108] G. Picard, A. Ajdari, F. Lequeux, and L. Bocquet, Elastic consequences of a single plastic event: A step towards the microscopic modeling of the flow of yield stress fluids, *The European Physical Journal E* **15**, 371 (2004).
- [109] C. Monthus and J.-P. Bouchaud, Models of traps and glass phenomenology, *Journal of Physics A: Mathematical and General* **29**, 3847–3869 (1996).
- [110] A. Heuer, B. Doliwa, and A. Saksengwijit, Potential-energy landscape of a supercooled liquid and its resemblance to a collection of traps, *Phys. Rev. E* **72**, 021503 (2005).
- [111] C. Liu, E. E. Ferrero, F. Puosi, J.-L. Barrat, and K. Martens, Driving Rate Dependence of Avalanche Statistics and Shapes at the Yielding Transition, *Physical Review Letters* **116**, 065501 (2016).
- [112] As we discuss in Sec. II, fast particles relax mainly through thermal activation rather than shear. However, it does not mean that the microscopic configuration of fast particles does not distort. As seen from Ref. [42] and some theoretical studies, such as J. F. Schwarzl and S. Hess, Shear-flow-induced distortion of the structure of a fluid: Application of a simple kinetic equation, *Phys. Rev. A* **33**, 4277 (1986); and S. Hess and H. Hanley, Stokes-maxwell relations for the distorted fluid microstructure, *Physics Letters A* **98**, 35–38 (1983), the cage is distorted even the shear is weak and the collective elasticity is absent.
- [113] J. F. Schwarzl and S. Hess, Shear-flow-induced distortion of the structure of a fluid: Application of a simple kinetic equation, *Phys. Rev. A* **33**, 4277 (1986).
- [114] S. Hess and H. Hanley, Stokes-maxwell relations for the distorted fluid microstructure, *Physics Letters A* **98**, 35–38 (1983).
- [115] J. O. Cochran, G. L. Callaghan, M. J. G. Caven, and S. M. Fielding, Slow Fatigue and Highly Delayed Yielding via Shear Banding in Oscillatory Shear, *Physical Review Letters* **132**, 168202 (2024).
- [116] J. Ding, Y.-Q. Cheng, H. Sheng, M. Asta, R. O. Ritchie, and E. Ma, Universal structural parameter to quantitatively predict metallic glass properties, *Nature Communications* **7**, 13733 (2016).
- [117] Q. Wang, L.-F. Zhang, Z.-Y. Zhou, and H.-B. Yu, Predicting the pathways of string-like motions in metallic glasses via path-featurizing graph neural networks, *Science Advances* **10**, eadk2799 (2024).
- [118] G. Jung, G. Biroli, and L. Berthier, Predicting Dynamic Heterogeneity in Glass-Forming Liquids by Physics-Inspired Machine Learning, *Physical Review Letters* **130**, 238202 (2023).
- [119] R. M. Alkemade, F. Smalenburg, and L. Filion, Improving the prediction of glassy dynamics by pinpointing the local cage, *The Journal of Chemical Physics* **158**, 134512 (2023).
- [120] Z. Wang, T. Iwashita, L. Porcar, Y. Wang, Y. Liu, L. E. Sánchez-Díaz, B. Wu, G.-R. Huang, T. Egami, and W.-R. Chen, Local elasticity in nonlinear rheology of interacting colloidal glasses revealed by neutron scattering and rheometry, *Physical Chemistry Chemical Physics* **21**, 38–45 (2019).
- [121] A. Furukawa, Quantification of the volume-fraction reduction of sheared fragile glass-forming liquids and its impact on rheology, *Physical Review Research* **5**, 023181 (2023).
- [122] A. Furukawa, Onset of shear thinning in glassy liquids: Shear-induced small reduction of effective density, *Physical Review E* **95**, 012613 (2017).
- [123] Z. Zhang and W. Kob, Revealing the three-dimensional structure of liquids using four-point correlation functions, *Proceedings of the National Academy of Sciences* **117**, 14032 (2020).
- [124] N. Singh, Z. Zhang, A. K. Sood, W. Kob, and R. Ganapathy, Intermediate-range order governs dynamics in dense colloidal liquids, *Proceedings of the National Academy of Sciences* **120**, e2300923120 (2023).
- [125] I. Tah, S. Sengupta, S. Sastry, C. Dasgupta, and S. Karmakar, Glass Transition in Supercooled Liquids with Medium-Range Crystalline Order, *Physical Review Letters* **121**, 085703 (2018).
- [126] C. W. Ryu and T. Egami, Medium-range atomic correlation in simple liquids. i. distinction from short-range order, *Phys. Rev. E* **104**, 064109 (2021).
- [127] H. W. Sheng, W. K. Luo, F. M. Alamgir, J. M. Bai, and E. Ma, Atomic packing and short-to-medium-range order in metallic glasses, *Nature* **439**, 419 (2006).
- [128] H. Tong and H. Tanaka, Structural order as a genuine control parameter of dynamics in simple glass formers, *Nature Communications* **10**, 5596 (2019).
- [129] S. Marín-Aguilar, H. H. Wensink, G. Foffi, and F. Smalenburg, Tetrahedrality Dictates Dynamics in Hard Sphere Mixtures, *Physical Review Letters* **124**, 208005 (2020).
- [130] F. Pedregosa, G. Varoquaux, A. Gramfort, V. Michel, B. Thirion, O. Grisel, M. Blondel, P. Prettenhofer, R. Weiss, V. Dubourg, J. Vanderplas, A. Passos, D. Cournapeau, M. Brucher, M. Perrot, and E. Duchesnay, Scikit-learn: Machine learning in Python, *Journal of Machine Learning Research* **12**, 2825 (2011).
- [131] R. A. Denny, D. R. Reichman, and J.-P. Bouchaud, Trap Models and Slow Dynamics in Supercooled Liquids, *Physical Review Letters* **90**, 025503 (2003).
- [132] D. J. Lacks and M. J. Osborne, Energy landscape picture of overaging and rejuvenation in a sheared glass, *Phys. Rev. Lett.* **93**, 255501 (2004).
- [133] D. J. Lacks, Energy Landscapes and the Non-Newtonian Viscosity of Liquids and Glasses, *Physical Review Letters* **87**, 225502 (2001).
- [134] M. Pica Ciamarra, W. Ji, and M. Wyart, Local vs. cooperative: Unraveling glass transition mechanisms with SEER, *Proceedings of the National Academy of Sciences* **121**, e2400611121 (2024).

- [135] W. Ji, M. Pica Ciamarra, and M. Wyart, The role of excitations in supercooled liquids: Density, geometry, and relaxation dynamics, *Proceedings of the National Academy of Sciences* **122**, e2416800122 (2025).
- [136] D. J. Wales, A microscopic basis for the global appearance of energy landscapes, *Science* **293**, 2067–2070 (2001).
- [137] C. E. Maloney and D. J. Lacks, Energy barrier scalings in driven systems, *Physical Review E* **73**, 061106 (2006).
- [138] P. Sollich, Rheological constitutive equation for a model of soft glassy materials, *Physical Review E* **58**, 738 (1998).
- [139] Y. Suzuki, J. Haimovich, and T. Egami, Bond-orientational anisotropy in metallic glasses observed by x-ray diffraction, *Phys. Rev. B* **35**, 2162 (1987).
- [140] J. Dong, H. Peng, H. Wang, Y. Tong, Y. Wang, W. Dmowski, T. Egami, B. Sun, W. Wang, and H. Bai, Non-affine atomic rearrangement of glasses through stress-induced structural anisotropy, *Nature Physics* **10.1038/s41567-023-02243-9** (2023).
- [141] H. J. Hwang, R. A. Riggleman, and J. C. Crocker, Understanding soft glassy materials using an energy landscape approach, *Nature Materials* **15**, 1031 (2016).
- [142] E. Agoritsas, E. Bertin, K. Martens, and J.-L. Barrat, On the relevance of disorder in athermal amorphous materials under shear, *The European Physical Journal E* **38**, 71 (2015).
- [143] R. N. Chacko, F. P. Landes, G. Biroli, O. Dauchot, A. J. Liu, and D. R. Reichman, Elastoplasticity Mediates Dynamical Heterogeneity Below the Mode Coupling Temperature, *Physical Review Letters* **127**, 048002 (2021).
- [144] T. S. Ingebrigtsen, T. B. Schröder, and J. C. Dyre, What Is a Simple Liquid?, *Physical Review X* **2**, 011011 (2012).
- [145] P. H. Poole, F. Sciortino, U. Essmann, and H. E. Stanley, Phase behaviour of metastable water, *Nature* **360**, 324 (1992).
- [146] A. K. Soper and M. A. Ricci, Structures of High-Density and Low-Density Water, *Physical Review Letters* **84**, 2881 (2000).
- [147] J. C. Palmer, F. Martelli, Y. Liu, R. Car, A. Z. Panagiotopoulos, and P. G. Debenedetti, Metastable liquid–liquid transition in a molecular model of water, *Nature* **510**, 385 (2014).
- [148] Z. Wang, K. Ito, J. B. Leão, L. Harriger, Y. Liu, and S.-H. Chen, Liquid–Liquid Phase Transition and Its Phase Diagram in Deeply-Cooled Heavy Water Confined in a Nanoporous Silica Matrix, *The Journal of Physical Chemistry Letters* **6**, 2009 (2015).
- [149] P. Gallo, K. Amann-Winkel, C. A. Angell, M. A. Anisimov, F. Caupin, C. Chakravarty, E. Lascaris, T. Lörting, A. Z. Panagiotopoulos, J. Russo, J. A. Sellberg, H. E. Stanley, H. Tanaka, C. Vega, L. Xu, and L. G. M. Pettersson, Water: A Tale of Two Liquids, *Chemical Reviews* **116**, 7463 (2016).
- [150] K. H. Kim, K. Amann-Winkel, N. Giovambattista, A. Späh, F. Perakis, H. Pathak, M. L. Parada, C. Yang, D. Mariedahl, T. Eklund, Thomas. J. Lane, S. You, S. Jeong, M. Weston, J. H. Lee, I. Eom, M. Kim, J. Park, S. H. Chun, P. H. Poole, and A. Nilsson, Experimental observation of the liquid-liquid transition in bulk supercooled water under pressure, *Science* **370**, 978 (2020).
- [151] K. Kapoor, Amandeep, and S. Patil, Viscoelasticity and shear thinning of nanoconfined water, *Physical Review E* **89**, 013004 (2014).
- [152] I. De Almeida Ribeiro and M. De Koning, Non-Newtonian flow effects in supercooled water, *Physical Review Research* **2**, 022004 (2020).
- [153] F. H. Stillinger, Phase transitions in the Gaussian core system, *The Journal of Chemical Physics* **65**, 3968 (1976).
- [154] A. Jusufi and C. N. Likos, *Colloquium* : Star-branched polyelectrolytes: The physics of their conformations and interactions, *Reviews of Modern Physics* **81**, 1753 (2009).
- [155] C. N. Likos, Soft matter with soft particles, *Soft Matter* **2**, 478 (2006).
- [156] A. A. Louis, P. G. Bolhuis, and J. P. Hansen, Mean-field fluid behavior of the Gaussian core model, *Physical Review E* **62**, 7961 (2000).
- [157] A. Ikeda and K. Miyazaki, Glass Transition of the Monodisperse Gaussian Core Model, *Physical Review Letters* **106**, 015701 (2011).